DEVELOPMENTAL BIOLOGY

A novel cardiomyogenic role for Isl1$^+$ neural crest cells in the inflow tract

Konstantinos E. Hatzistergos[1,2,3]*, Michael A. Durante[2,4,5], Krystalenia Valasaki[2], Amarylis C. B. A. Wanschel[2], J. William Harbour[2,4,5], Joshua M. Hare[2,5,6]

The degree to which populations of cardiac progenitors (CPCs) persist in the postnatal heart remains a controversial issue in cardiobiology. To address this question, we conducted a spatiotemporally resolved analysis of CPC deployment dynamics, tracking cells expressing the pan-CPC gene *Isl1*. Most CPCs undergo programmed silencing during early cardiogenesis through proteasome-mediated and PRC2 (Polycomb group repressive complex 2)–mediated Isl1 repression, selectively in the outflow tract. A notable exception is a domain of cardiac neural crest cells (CNCs) in the inflow tract. These "dorsal CNCs" are regulated through a Wnt/β-catenin/Isl1 feedback loop and generate a limited number of trabecular cardiomyocytes that undergo multiple clonal divisions during compaction, to eventually produce ~10% of the biventricular myocardium. After birth, CNCs continue to generate cardiomyocytes that, however, exhibit diminished clonal amplification dynamics. Thus, although the postnatal heart sustains cardiomyocyte-producing CNCs, their regenerative potential is likely diminished by the loss of trabeculation-like proliferative properties.

INTRODUCTION

Formation of the four-chambered, mature, adult mammalian heart involves a series of spatially and temporally controlled morphogenetic processes. Many of these organ-founding processes are controlled by gene regulatory networks expressing the transcription factor *Isl1*. Activation of Isl1 is originally detected during precardiac mesoderm specification (*1*, *2*). This Isl1$^+$ splanchnic mesoderm region will produce the two main cardiac progenitor cell (CPC) lineages, the first (FHF) and second (SHF) heart fields from which most contractile cardiomyocytes (CMs) will develop (*1*, *2*).

Specification of precardiac mesoderm into FHF CPCs requires inactivation of Isl1 and induction of the master cardiac transcription factor Nkx2-5 (*1*). The Isl1$^-$/Nkx2-5$^+$ FHF CPCs will then give rise into a linear, beating heart tube. This tube is patterned into a venous/inflow (IFT) and an arterial/outflow (OFT) pole along its anteroposterior axis and will later develop into the left ventricle (LV), parts of the atria, and interventricular septum (IVS) (*3*).

The SHF forms medially and dorsally to the FHF, from the splanchnic mesoderm region ventrally to the pharynx through mechanisms that require continued expression of Isl1 (*1*, *2*). The SHF is patterned to an anterior (aSHF) and posterior (pSHF) domain. aSHF- and pSHF-CPCs express *Isl1* through different cis-regulatory elements (*4*, *5*). In addition to Isl1, aSHF-CPCs coexpress Nkx2-5 and are deployed through the arterial pole of the heart tube to produce the right ventricle (RV), parts of the IVS, and OFT (*2*). The pSHF-CPCs are deployed through the venous pole and will give rise to the dorsal mesocardium, pulmonary and caval veins, and parts of the cardiac conduction system and atria (*3*). The recruitment of aSHF- and pSHF-CPCs through the arterial and venous poles, respectively, causes the linear heart tube to elongate, bend, and eventually undergo a rightward looping, which shifts its venous and arterial poles to their definitive positions ventrally (OFT) and dorsally (IFT) to the cardiac base, respectively (*3*).

After looping, the OFT and IFT become oriented along the dorsoventral rather than anteroposterior embryonic axis, and the heart enters its growth and maturation phase. A new layer of trabecular CMs grows along the endocardial surface of the ventricles, which later undergoes compaction and expands clonally into the IVS myocardium (*3*, *6*). Concurrently, neural ectoderm–derived cardiac neural crest cells (CNCs) are deployed from the rhombencephalon (*3*). In particular, an early wave of CNCs migrates through the pharyngeal arches into the OFT to primarily contribute to the aorticopulmonary septation and smooth muscle cells (SMCs), as well as parasympathetic innervation (*3*), whereas a second wave of apoptosis-prone CNCs is thought to migrate later through the pSHF-derived dorsal mesocardium into the IFT, to contribute sympathetic nerves and endocardial cushion mesenchyme (*7*–*9*). Notably, the new CMs that are produced during the trabeculation and compaction stages are thought to amplify from preexisting CMs (*6*). However, recent studies in mice (*10*, *11*), birds (*11*), and fish (*12*, *13*) indicate substantial trabecular CM contribution from CNCs as well. Expression of Isl1 marks CNCs in both the IFT and OFT, and loss of *Isl1* in mice produces SHF and CNC and trabecular defects (*2*, *14*).

Upon transition to the postnatal life, these organ-founding CPCs are thought to be depleted from the mammalian heart, thereby limiting its regenerative capacity. Regeneration of CMs is possible only during the early neonatal life likely through preexisting CM proliferation (*3*, *15*). However, expression of *Isl1* persists in few cells within the adult IFT, OFT, and sinoatrial node (SAN). Intriguingly, studies in rodents and humans indicate that some of the OFT postnatal Isl1 cells are aSHF-derived CPCs and could be therapeutically targeted for postnatal heart regeneration (*3*, *16*). On the other hand, complete regeneration of CMs in the postnatal univentricular fish heart involves the reactivation of fetal heart growth mechanisms,

[1]Aristotle University of Thessaloniki, Faculty of Sciences, School of Biology, Department of Genetics, Development and Molecular Biology, Thessaloniki 54124, Greece. [2]Interdisciplinary Stem Cell Institute, University of Miami Miller School of Medicine, Miami, FL 33136, USA. [3]Department of Cell Biology, University of Miami Miller School of Medicine, Miami, FL 33136, USA. [4]Bascom Palmer Eye Institute, University of Miami Miller School of Medicine, Miami, FL 33136, USA. [5]Sylvester Comprehensive Cancer Center, University of Miami Miller School of Medicine, Miami, FL 33136, USA. [6]Department of Medicine, University of Miami Miller School of Medicine, Miami, FL 33136, USA.
*Corresponding author. Email: kchatzistergos@bio.auth.gr, kchatzistergos@med.miami.edu

including proliferative expansion of trabecular (*17*) and CNC-derived CMs (*13*), as well as de novo cardiomyogenesis from CNCs (*11*). Accordingly, here, we investigate the mechanisms of cardiomyogenesis in the postembryonic mouse heart through a combination of *Isl1*-targeted, multicolor lineage-tracing and single-cell RNA sequencing (scRNAseq) experiments. Our results indicate that, indeed, the organ-founding CPCs are depleted in the postnatal mouse heart. However, a notable exception is a pool of CNC derivatives in the IFT region, which sustain Isl1 expression through a Wnt/β-catenin/Isl1 feedback loop and contribute to normal ventricular trabeculation and compaction. We further show that, developmentally, these "dorsal" Isl1$^+$ CNCs generate a limited number of trabecular CMs, which subsequently expand clonally during ventricular morphogenesis, eventually producing ~10% of the biventricular and IVS myocardium. After birth, Isl1$^+$ CNCs continue to generate limited amounts of biventricular CMs, which, however, lack clonal division capacity, and therefore, their ability to contribute to postnatal cardiomyogenesis is likely diminished.

RESULTS

Diverse developmental origins and identities of postnatal cardiac cells with sustained *Isl1* activity

To monitor the expression of the pan-CPC gene *Isl1*, we used a previously described mouse line carrying a *loxP*-flanked *Isl1-nLacZ* allele (fig. S1A) (*14*). This *Isl1-nLacZ* knock-in reports *Isl1* transcription from both neural and mesoderm-specific regulatory elements (*4*, *5*, *14*). Accordingly, as previously shown (*14*), *Isl1-nLacZ* is expressed in aSHF and pSHF CPCs during early cardiogenesis (fig. S1B) and later in CNCs (fig. S1C). After birth, its cardiac expression is sustained in five distinct dorsoventral domains (fig. S1, D and E). Ventrally (OFT), *Isl1-nLacZ* is expressed in cells within the proximal aorta (Ao) and pulmonary artery (PA), as well as the OFT myocardium (fig. S1D). Dorsally (IFT), *Isl1-nLacZ* labels cardiac ganglia (CGs) and the SAN (fig. S1E).

The OFT develops from aSHF-CPCs and CNCs that are primarily recruited through the arterial pole of the heart tube (*14*, *18*), whereas the IFT develops from pSHF-CPCs (including the SAN) and CNCs that are primarily recruited through the venous pole of the heart tube (*7*–*9*, *14*). Therefore, to determine the lineage of the cells that comprise the ventral and dorsal postnatal *Isl1-nLacZ*$^+$ domains, we interbred the *Isl1-nLacZ* to the aSHF-specific *MEF2c-AHF-Cre* and CNC-specific *Wnt1-Cre2* mouse lines. Under this strategy, the *loxP*-flanked *Isl1-nLacZ* reporter is conditionally excised from aSHF- and CNC-derived heart cells, respectively. Consequently, expression of *Isl1-nLacZ* persists in nonrecombined cell lineages (fig. S2A).

As expected, in *Isl1-nLacZ;Mef2c-AHF-Cre* neonatal hearts (*nLacZ* excision from aSHF) the dorsal x-gal signal is not affected, indicating that the dorsal *Isl1-nLacZ*$^+$ cells are not aSHF derivatives (fig. S2, B to E). However, the ventral x-gal signal diminishes by ~7-fold ($P < 0.0005$), indicating that most, but not all, ventral *Isl1-nLacZ*$^+$ cells are aSHF derivatives (fig. S2, B, C, and N). Immunohistochemical analysis of the remaining x-gal$^+$ cells in the ventral *Isl1-nLacZ*$^+$ domain indicates that these are mostly SM22a$^+$ SMCs and tyrosine hydroxylase–positive (TH)$^+$ sympathetic neurons within the proximal PA and Ao. Unexpectedly, few α-sarcomeric actinin$^+$/x-gal$^+$ CMs within the OFT myocardium are also present, indicating that non-aSHF–derived cells contribute a minority of ventral *Isl1-nLacZ*$^+$ CMs in this region (figs. S2, B and C, and S3, A to E).

Comparably, in *Isl1-nLacZ;Wnt1-Cre2* neonatal hearts (*nLacZ* excision from CNCs), the ventral x-gal signal is minimally reduced, indicating that only a small fraction of the ventral *Isl1-nLacZ*$^+$ cells are CNC derivatives (fig. S2, F, G, and N). This finding confirms previous reports that Isl1$^+$ cells of both aSHF and CNC origin contribute to the OFT (*14*, *18*). The dorsal x-gal signal is not affected in the SAN, but, as expected, x-gal is extinguished from the CNC-derived CGs (fig. S2, H, I, and N).

In triple-mutant *Isl1-nLacZ;Wnt1-Cre2;Mef2c-AHF-Cre* mice (*nLacZ* excision from both aSHF and CNCs), x-gal is sustained in few sm22a$^+$ SMCs in the proximal PA and the dorsolateral wall of the Ao but is extinguished from TH$^+$ neurons and α-sarcomeric actinin$^+$ CMs (figs. S2, J, K, and N, and S3F). This indicates that, in addition to the previously identified CNC and aSHF contributions (*14*, *18*), there is a third lineage that also contributes Isl1$^+$ SMCs in the postnatal OFT. On the basis of previous reports (*19*), we postulate that these cells likely belong to the pSHF lineage, although further pSHF-specific lineage-tracing studies are required to confirm this hypothesis. Last, as expected, the dorsal x-gal signal is not affected in the pSHF-derived SAN but is extinguished from the CNC-derived CGs (figs. S2, L to N, and S3G). Collectively, these *Isl1-nLacZ* lineage-tracing experiments expand upon previous work (*14*, *18*), by delineating that sustained activity of *Isl1* in the postnatal IFT region identifies CNC-derived cells and the SAN, whereas *Isl1-nLacZ* activity in the postnatal OFT region identifies a mixture of CNC-derived TH$^+$ neurons, OFT CMs (most of which derive from the aSHF and some from the CNC), and SMCs in the proximal PA and Ao, which descend from at least three distinct developmental origins.

Ventral but not dorsal *Isl1* is transcriptionally silenced

By postnatal (PN) week 4, *Isl1-nLacZ* activity in the OFT has diminished (fig. S1, D, F, and H). In particular, x-gal signal is reduced in the PA and virtually extinguished from the OFT base and Ao, except from a few cells in the dorsolateral Ao wall medially to the SAN (fig. S1, D, F, H, and J). No remarkable changes are observed in dorsal (SAN and CG) *Isl1-nLacZ* activity (fig. S1, E and F to I).

To understand what causes the progressive loss in postnatal *Isl1-nLacZ* activity selectively in the OFT but not IFT region, we dissected the dorsal (including the SAN and CGs) and ventral (including the Ao, PA, and OFT base) domains of the cardiac base from *Isl1*$^{+/+}$ neonatal mice, dissociated them into single-cell suspensions, recovered them in culture for 5 days, and processed them for scRNAseq (Fig. 1A). A total of 11,418 ventral and 9893 dorsal cells were sequenced. Analysis of transcriptional identities by Uniform Manifold Approximation and Projection (UMAP) dimensional reduction generated a total of 15 transcriptionally and spatially distinct clusters (Fig. 1, B to D, and data S1A). To classify the clusters, we first performed an unbiased gene set enrichment analysis (GSEA) of cluster-specific genes, and the resulting cell types were elaborated further by profiling the expression of 48 canonical marker genes (Fig. 1, C and D). Accordingly, cluster 0 is enriched in *Sox9*, *Fbn1*, and *Nfatc1* and is therefore assigned a cardiac valve cell identity. Clusters 1, 2, and 5 are enriched in *Fap* and are therefore classified as fibroblasts. Cluster 3 is enriched in Wt1 and is therefore assigned an epicardial identity. Clusters 4, 6, and 8 are enriched in *Myh11 and Tagln* and are therefore classified as SMCs. Cluster 7 is classified as CNC-derived cells based on the expression of *Sox2*, *Sox10*, *Plp1*, *Nes*, *Ngfr*, *Foxd3*, and *Tfap2a*. Cluster 9 is enriched in *Pecam1*, *Cdh5*, *Kit*, *Kdr*, and *Nr2f2* and is therefore classified as venous endothelium.

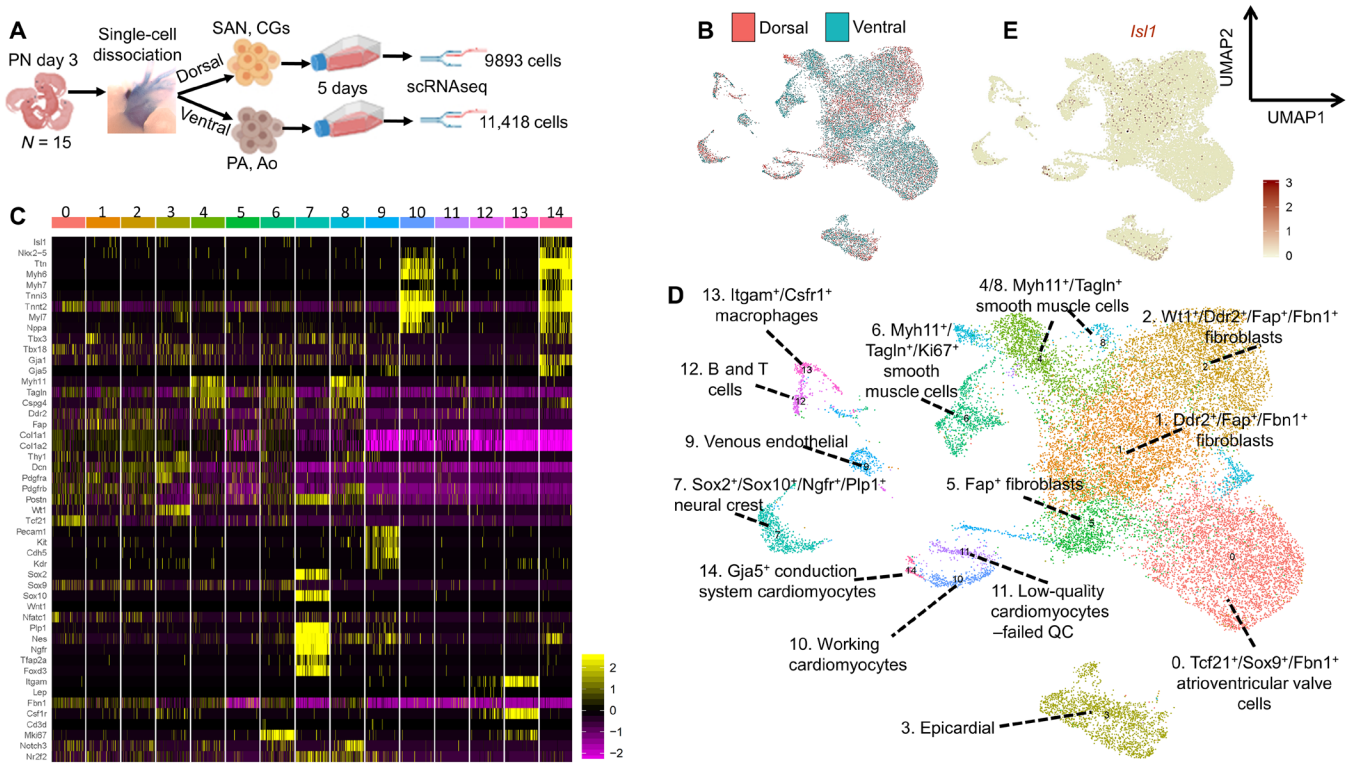

Fig. 1. scRNAseq of arterial (ventral) and venous (dorsal) pole–derived neonatal cells. (**A**) Experimental outline. (**B**) UMAP dimensional reduction plot of 21,311 scRNAseq profiles following integration of the postnatal (PN) day 3 dorsal and ventral datasets. (**C**) Heatmap of 47 lineage-specific genes across the 15 UMAP clusters. For visualization, each cluster is downsampled to 100 cells. (**D**) UMAP plot of classified cell clusters. (**E**) Expression of Isl1, visualized on UMAP plots. QC, quality control.

Cluster 10 is assigned a working myocardial cell identity based on the expression of *Nkx2-5*, *Myh6*, *Myh7*, *Ttn*, *Tnni3*, *Tnnt2*, *Myl7*, and *Nppa*. Cluster 11 is identified as low-quality/dying ventricular CMs due to high mitochondrial contamination (data S1A). Clusters 12 and 13 are classified as immune cells (B/T lymphocytes and macrophages, respectively), and lastly, cluster 14 is identified as conduction system CMs (which include the dorsal cluster of *nkx2-5*–negative/*Isl1*$^+$ SAN CMs), based on the expression of *Isl1*, *Gja5*, *Ttn*, *Tnnt2*, and *Myh7*. None of the clusters showed enrichment for *Isl1* expression (Fig. 1, C to E). Rather, *Isl1*-expressing cells were present in 14 of the 15 clusters, revealing a remarkable diversity of postnatal *Isl1*$^+$ cardiac cells (Fig. 1E).

Next, the *Isl1*$^+$ cells were subselected from the scRNAseq datasets on the basis of their dorsoventral identities and subjected to differential gene expression (DEG) analysis (Fig. 2A). Overall, there were 278 ventral and 205 dorsal *Isl1*$^+$ cells with 567 DEGs (Fig. 2B and data S1B). Functional enrichment analyses showed overrepresentation of multiple terms, including biological processes related to heart and CNC development, regulation of transcription, and PRC2 (Polycomb group repressive complex 2)–related gene silencing [embryonic ectoderm development (Eed) and suppressor of zeste 12 (Suz12)] (Fig. 2, C and D, and data S2, A and B). Previous studies have demonstrated that cardiac PRC2—which consists of three core subunits: Eed, Suz12, and either enhancer of zeste 1 or 2 (Ezh1 or Ezh2)—plays an essential role in normal heart development by directly repressing the expression of cell cycle inhibitors, such as *Ink4a/b*, as well as early skeletal muscle and neuronal genes, including *Pax6*, *Six1*, and *Isl1*, to facilitate proper expression of CM differentiation and proliferation genes (*20*). We therefore hypothesized that PRC2-mediated transcriptional silencing of the *Isl1* gene underlies the loss of ventral *Isl1-nLacZ* activity. To functionally test this possibility, we cultured cells from the OFT *Isl1* domain of PN week 4 *Isl1-nLacZ* hearts (in which *Isl1-nLacZ* activity has already diminished; i.e., fig. S1) for 5 days in the presence or absence of EED226, an allosteric small-molecule PRC2 inhibitor targeting the H3K27me3 binding pocket of Eed (Fig. 2E) (*21*). Western blot and immunocytochemical analyses confirmed the successful inhibition of PRC2 activity in EED226-treated cells, as shown by the down-regulation in H3K27me3 levels compared to controls (Fig. 2F). Gene expression and x-gal analyses showed that inhibition of PRC2-mediated H3K27me3 in ventral cells resulted in significant recovery in *Isl1* mRNA transcription (Fig. 2G) and reactivation of the *Isl1-nLacZ* reporter (Fig. 2, H and I), respectively. Thus, on the basis of the above findings, we conclude that *Isl1-nLacZ* activity is progressively lost in the postnatal OFT, but not IFT region, and that erasure of PRC2-mediated H3K27me3-repressive histone modifications in postnatal OFT cells results in significant recovery in both x-gal and *Isl1* mRNA levels.

When we analyzed the occupancy of the *Isl1* gene and its known regulatory elements by H3K27me3 and H3K27ac in chromatin immunoprecipitation sequencing (ChIP-seq) datasets from whole embryonic and postnatal *Isl1*$^{+/+}$ mouse hearts, we detected H3K27me3 peaks as early as embryonic day 10.5 (E10.5) on the promoter and heart field–specific enhancer regions, whereas the peaks of the transcriptional activator H3K27ac on the promoter region were virtually diminished by E14.5 (fig. S4). These observations are in agreement

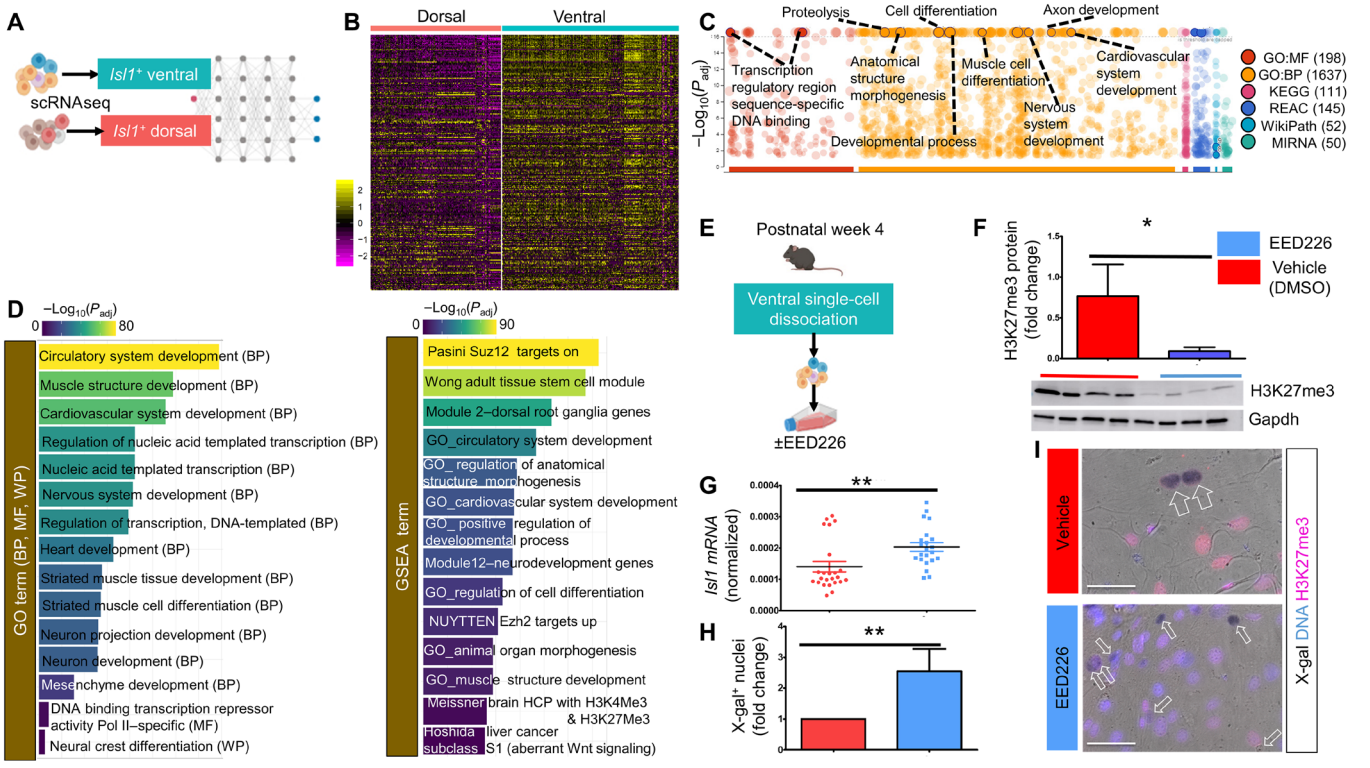

Fig. 2. PRC2-mediated transcriptional silencing of ventral postnatal *Isl1* expression. (**A**) Experimental outline. (**B**) Heatmap of the top 250 DEGs (Wilcoxon rank sum test) between the dorsal and ventral *Isl1*$^+$ cells (*P* value adjustment was performed using Bonferroni correction based on the total number of genes in the dataset). (**C**) Functional profiling of DEGs (false discovery rate–adjusted $P < 0.05$), visualized in a Manhattan-like plot. Functional terms are grouped and color-coded by data sources (total number of terms per source shown in parenthesis). The g:SCS algorithm was applied for multiple testing correction of the adjusted enrichment *P* values shown here in negative $\log_{10}$ scale [$-\log10(P_{adj})$]. Values are capped at $-\log_{10}(P_{adj}) \leq 16$. Examples of some of the most significant terms are noted. (**D**) Bar graphs of overrepresented Gene Ontology (GO; left) and GSEA (right) terms. The scale of $-\log_{10}(P_{adj})$ values is numeric and color coded. (**E**) Experimental outline of PRC2 inhibition. (**F**) Western blots of Gapdh and H3K27me3, 5 days after treatment with DMSO or 10 μM EED226. *$P = 0.04$, paired *t* test. (**G** and **H**) Quantification of *Isl1* mRNA (G, **$P = 0.0046$, paired *t* test) and x-gal$^+$ nuclei/group (H, **$P = 0.0097$, Mann Whitney test). (**I**) x-gal and H3K27me3 staining. (F to I) $n = 24$ samples from four mice (12 samples per group). For quantitative PCR, a technical replicate was included per run. Scale bars, 150 μm. BP, biological process; GO, gene ontology; KEGG, Kyoto Encyclopedia of Genes and Genomes; MF, molecular function; MIRNA, microRNAs; REAC, Reactome; WP, Wikipathways.

with previous genetic screens for *Isl1* enhancers in transgenic reporter mice, showing permanent silencing of the heart field–specific *Isl1* enhancers after early cardiogenesis (*5*). Moreover, they indicate that the *Isl1-nLacZ* reporter gene activity and *Isl1* mRNAs that we detected in the postnatal mouse heart are produced through alternative, noncardiac elements of the gene, which is unexpected given our previous observation that ~80% of the postnatal *Isl1-nLacZ*$^+$ OFT cells are aSHF derivatives (fig. S2). Analysis of the more distal, neural-specific, regulatory elements showed no H3K27me3 occupancy, thereby corroborating the interpretation that cardiac *Isl1* transcriptional regulation is permanently switched to noncardiac regulatory elements upon transition from the embryonic to the fetal and postnatal life (fig. S4).

Ventral, but not dorsal, Isl1 is translationally silenced after early cardiogenesis

We further observed that, compared to the IFT, *Isl1-nLacZ* cells in the fetal and postnatal OFT exhibit complete lack of Isl1 immunoreactivity, indicating that OFT Isl1 expression is further regulated at the posttranscriptional level (Fig. 3, A and B). Because previous studies have suggested that Isl1 immunoreactivity differs between mouse strains (*22*), we confirmed the lack of Isl1 immunoreactivity in human fetal OFTs (fig. S5).

To understand the cause of the OFT-specific loss of Isl1 protein expression, we evaluated the functional enrichment analysis of the *Isl1*$^+$ scRNAseq DEGs. Multiple microRNA (miRNA)–related Gene Ontology (GO) terms, including miR-1a and miRNA-17 that have been previously shown to play important roles in cardiac development, were overrepresented (Fig. 3C and data S2, A and B). miRNA-17, which is part of the miRNA 17 to 92 cluster, has been shown to directly silence *Isl1* in aSHF-CPCs during embryonic development (*23*). Because miRNA biogenesis, including miR-1a and miRNA 17 to 92, largely depends on the ribonuclease III nuclease *Dicer*, we conditionally knocked out (cKO) *Dicer* in postnatal *Isl1* cells to functionally test the potential involvement of miRNAs in posttranscriptional silencing of ventral Isl1 expression. To do so, we generated mice carrying a tamoxifen-inducible *Isl1-MerCreMer*, a floxed *Dicer*, and a *tdTomato Cre* reporter (*Isl1-MCM;Dicer*$^{Flox/Flox}$*;tdTomato*) and induced them with intraperitoneal tamoxifen injections at PN2, PN4, and PN6 (Fig. 3D). Excision of one or both *Dicer*$^{Flox/Flox}$ alleles in *Isl1-MCM* cells was confirmed by tdTomato expression, as well as by reverse transcription polymerase chain reaction (PCR) amplification of the wild-type, recombined, and nonrecombined floxed alleles. Confocal analysis at PN7 showed comparable OFT and IFT tdTomato labeling between *Isl1-MCM;Dicer*$^{Flox/Flox}$*;tdTomato* and *Isl1-MCM;Dicer*$^{Flox/+}$*;tdTomato* hearts. However, loss of *Dicer* was not sufficient to reconstitute

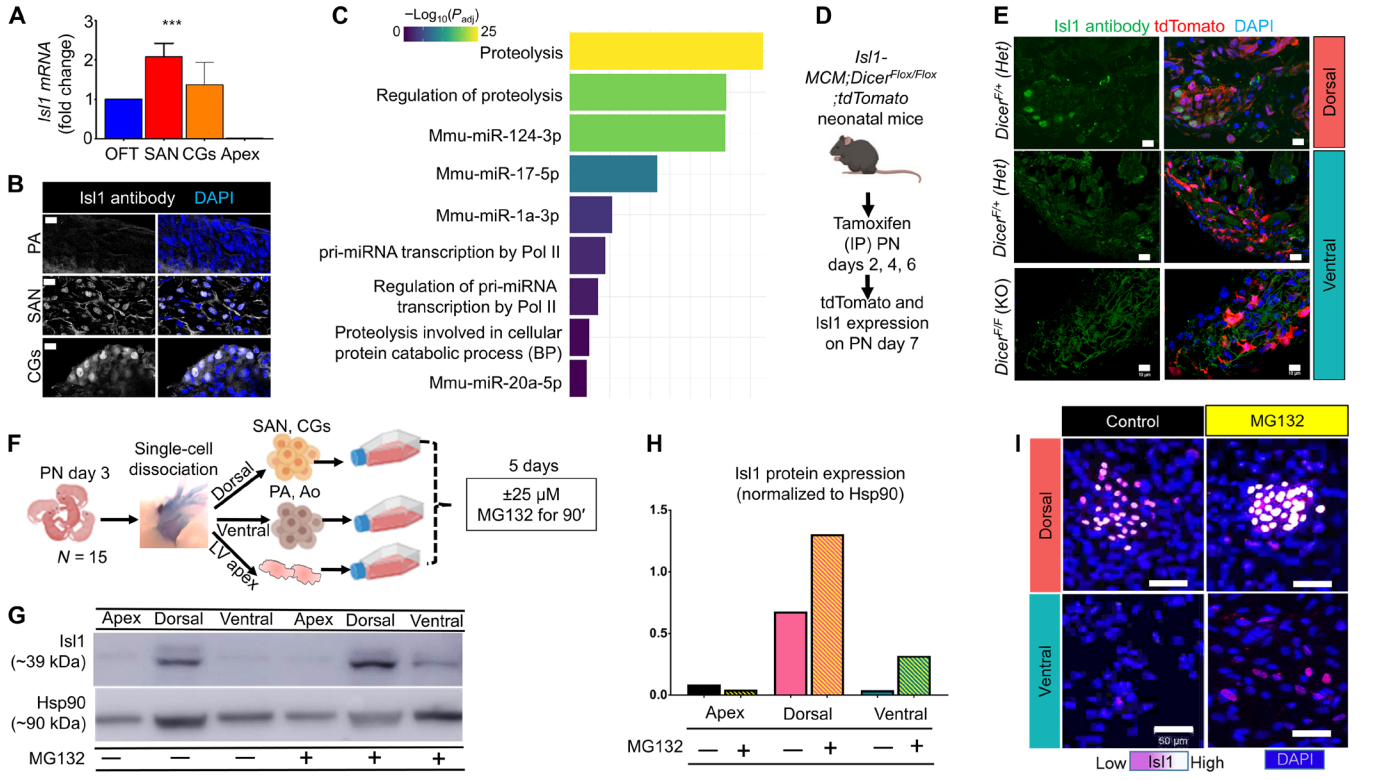

Fig. 3. Proteasomal degradation of ventral, but not dorsal, *Isl1* expression. (**A** and **B**) Ventral versus dorsal Isl1 mRNA (A) and protein (B) expression ($n = 5$ mice per group, ***$P < 0.0001$, one-way analysis of variance). DAPI, 4′,6-diamidino-2-phenylindole. (**C**) Bar graphs of overrepresented GO terms. The scale of $-\log_{10}(P_{adj})$ values is numeric and color coded. (**D** and **E**) Experimental design (D) and representative immunohistochemical analysis of Isl1 in *Isl1-MCM;Dicer*$^{Flox/Flox}$*;tdTomato* mice ($n = 4$ heterozygous; $n = 8$ Dicer-KO littermates). IP, intraperitoneal. (**F**) Illustration of the experimental outline to inhibit the ubiquitin-proteasome pathway in postnatal Isl1$^+$ domains. (**G** and **H**) Western blot analysis of Isl1 and Hsp90. (**I**) Immunofluorescent analysis of Isl1. n = pool of 15 mice per group. Scale bars, 10 μm (B and E) and 50 μm (I).

ventral Isl1 immunoreactivity (Fig. 3E). Thus, on the basis of these findings, we conclude that silencing of Isl1 protein expression in the postnatal OFT is not mediated by *Dicer*-processed miRNAs.

In addition to miRNAs, the *Isl1*$^+$ scRNAseq DEGs are enriched in multiple processes related to proteolysis (Figs. 2C and 3C and data S2, A and B). Notably, regulation of Isl1 protein stability and degradation has been shown to be essential for the establishment and differentiation of the aSHF in mouse embryos (*24*). Accordingly, cells from the left ventricular apex (negative control for Isl1) and from dorsal domains (positive control for Isl1) and ventral domains of PN3 *Isl1*$^{+/+}$ hearts were isolated and treated for 90 min with 25 μM ubiquitin-proteasome inhibitor MG132 (*N*-carbobenzyloxy-L-leucyl-L-leucyl-L-leucinal) or vehicle [DMSO (dimethyl sulfoxide)] (Fig. 3F). MG132-mediated inhibition of proteasomal degradation was sufficient to reconstitute ventral Isl1 protein expression as demonstrated by Western blot (Fig. 3, G and H) and immunocytochemical analyses (Fig. 3I). Collectively, these experiments show that, in addition to its transcriptional silencing, Isl1 expression is posttranslationally silenced in the postnatal OFT and that inhibition of the ubiquitin-proteasome pathway, but not *Dicer-cKO*, results in the recovery of Isl1 protein expression in postnatal OFT cells.

Isl1$^+$ CNCs contribute septal and trabecular CMs that undergo proliferative expansion in the pre- but not postembryonic mouse heart

Previous studies in mice suggest that some postnatal *Isl1*$^+$ OFT cells are undifferentiated aSHF CPCs (*16*). Others, however, provide evidence against it (*15*). To gain insight into this controversy, *Isl1-MCM* mice were crossed to the *tdTomato* or the dual-fluorescent *IRG* (*10*) reporter mice and induced with a single dose of tamoxifen at PN2. Analysis 48 hours later showed that *Isl1-MCM* recombination was partial compared to the *Isl1-nLacZ*, because it selectively labeled the dorsal (SAN and CGs) but not ventral (OFT) Isl1$^+$ cells. Therefore, to capture the ventral *Isl1*$^+$ cells, we repeatedly administered tamoxifen on PN2 and PN4 and extended the period of fate mapping to 2 weeks. Following this approach, comparable *Isl1-MCM* recombination was achieved in both domains, like the *Isl1-nLacZ*.

Compared to the *Isl1-nLacZ*, *Isl1-MCM* hearts exhibited widespread labeling in TH$^+$ neurons (Fig. 4, A to G), indicating that postnatal Isl1$^+$ cells contribute extensively to the postnatal growth of the cardiac sympathetic nervous system, which is a CNC derivative. Moreover, compared to the *Isl1-nLacZ* reporter, which only labels *Isl1*-expressing CMs within the OFT base myocardium (fig. S3, A and B), *Isl1-MCM* fate mapping marked rare, isolated, tdTomato$^+$ ventricular CMs, scattered within the compact and trabecular LV, RV, and IVS myocardium (Fig. 4, H to J). This finding corroborates previous studies suggesting that postnatal Isl1$^+$ cells maintain a progenitor cell state (*16*). However, it further highlights that postnatal Isl1$^+$ cells primarily contribute to TH$^+$ neurogenesis, whereas their contribution in CMs is minimal.

Intriguingly, we noticed that the rarely produced *Isl1-MCM* CMs were occasionally found adjacent to *Isl1-MCM* TH$^+$ nerves (Fig. 4, I and J). This observation, along with the finding that a subset of *Isl1-nLacZ*$^+$ OFT base CMs likely originate from the CNC

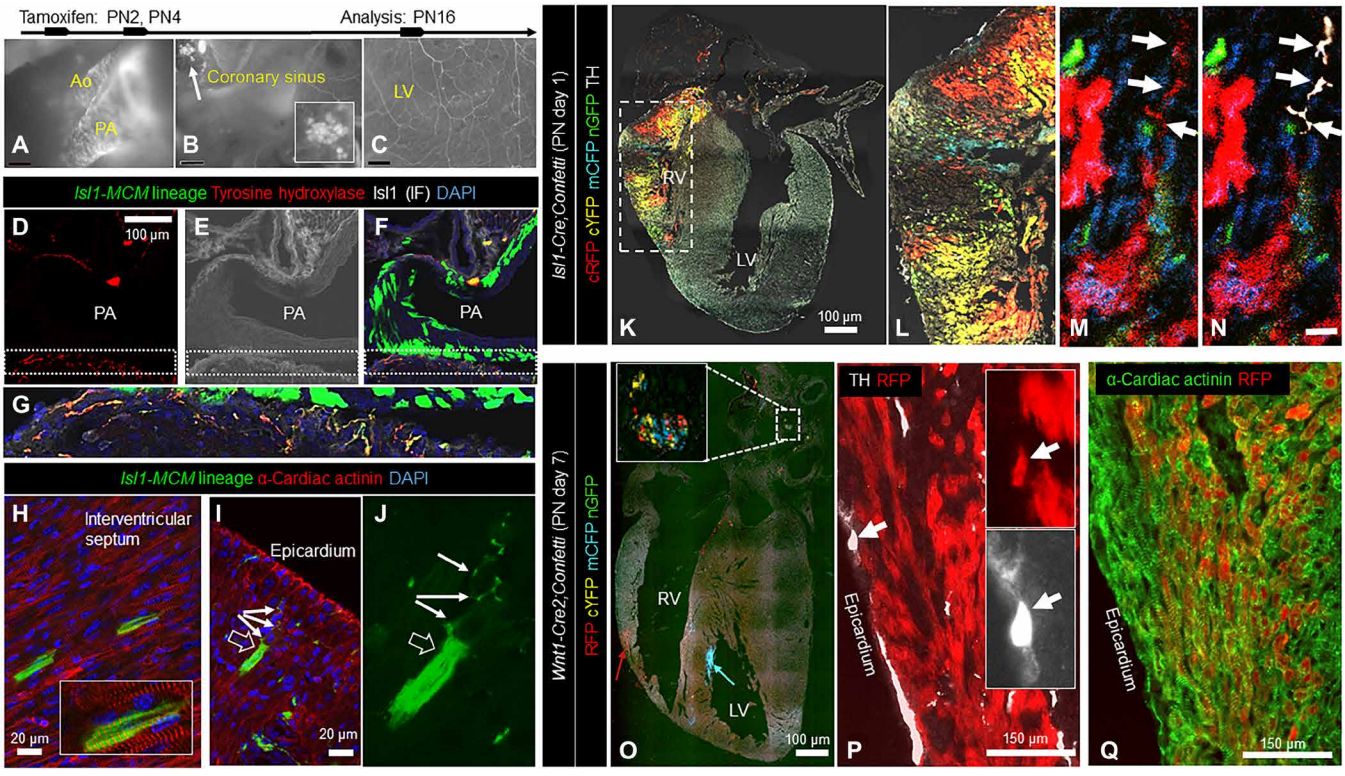

Fig. 4. *Isl1*$^+$ CNCs generate trabecular and septal CMs with pre- but not postnatal proliferative expansion capacity. (**A** to **C**) Live imaging of postnatal *Isl1-MCM; tdTomato* recombination in (A) the Ao, and PA, (B) CGs (arrow and inset), and (C) sympathetic nerves. (**D** to **F**) *Isl1-MCM;tdTomato* PA cells are immunoreactive to TH but not Isl1 antibodies. Panels D to F printed at identifcal magnification. (**G**) Higher magnification of the boxed area in (F). (**H** to **J**) Postnatal *Isl1-MCM;tdTomato* recombination in α-cardiac actinin$^+$ CMs within the IVS (H) and ventricles (I and J; J shows an nl). Note the proximity between the *Isl1-MCM;tdTomato*$^+$ CM (I and J) (empty arrow) and axon (I and J) (filled arrows). (**K** and **L**) Inefficient *Isl1-Cre;Confetti* recombination in TH$^+$ cells ($n = 7$ mice). (**M** and **N**) A red TH$^+$ neuron (arrows) within a red *Isl1-Cre;Confetti* myocardial clone. (**O**) *Wnt1-Cre2;Confetti* hearts exhibit proper recombination in CGs (inset) and ventricular myocardium (arrows). RFP, red fluorescent protein. (**P** and **Q**) Higher magnification of the red clone illustrates the presence of red CMs and TH$^+$ neurons, suggesting clonal origin of the two derivatives ($n = 35$ mice). For each *Confetti* heart, we evaluated 5 to 10 cryosections and two to three large, compact, unicolored myocardial clones (>10 cells) per cryosection. Scale bars, 100 μM (A to F, K, and O), 10 μM (N), 20 μM (H to J), and 150 μM (P and Q). IF, immunofluorescence.

(figs. S2 and S3) and that aSHF-specific *Isl1* regulatory elements are silenced in the postnatal heart (fig. S4), led us to hypothesize that the neonatal *Isl1-MCM* CMs are *Isl1*$^+$ CNC derivatives. Previous studies have demonstrated that murine CNCs are multipotent and can undergo differentiation into both neural and non-neural derivatives (*9*). Moreover, contributions of CNCs to the myocardial lineage have been previously shown in fish and birds (*11*, *12*) but is a topic of ongoing debate in mice (*10*, *11*).

Accordingly, to test the possibility that CMs and TH$^+$ neurons are derived from bipotent Isl1$^+$ CNCs, we first performed clonal analysis of *Isl1*$^+$ cardiac cells and their derivatives by crossing the *Isl1-Cre* to the multicolor Cre-reporter mouse line *Confetti* (Fig. 4K). As expected (*2*, *14*), analysis of PN1 *Isl1-Cre;Confetti* hearts showed extensive labeling in the compact and trabecular RV myocardium in the form of multiple, single-colored CM clusters of various sizes (Fig. 4, K to N). However, some segments of the RV myocardium were not labeled by the *Confetti* (Fig. 4, K and L). In addition, compared to the *Isl1-MCM;tdTomato* hearts, which exhibit widespread labeling in TH$^+$ neurons (Fig. 4, A to G), *Isl1-Cre;Confetti* hearts exhibited minimal labeling in TH$^+$ neurons (Fig. 4, K and L). These observations suggest that a substantial amount of cells escape fluorescent reporter labeling, likely because *Isl1-Cre* expression is not sufficiently strong to recombine the *Confetti* (*25*). Notably, same-color TH$^+$ neuron-CM pairs could be rarely detected within the RV, a finding that is potentially consistent with bipotency of CNC progenitors (Fig. 4, M and N). However, given the limited TH$^+$ labeling efficiency, which precludes any statistical assessment of CNC bipotency, in addition to the highly migratory nature of CNCs and the high clonal densities in the *Isl1-Cre;Confetti* RVs (Fig. 4, K and L), the possibility that these rare, same-color TH$^+$ neuron-CM pairs may have resulted from clone intermixing rather than differentiation of bipotent Isl1$^+$ CNCs cannot be excluded.

To overcome the *Isl1-Cre;Confetti* labeling limitations, we repeated the clonal analysis by replacing the *Isl1-Cre* with the neural crest–specific *Wnt1-Cre2* (Fig. 4, O to Q). Compared to *Isl1-Cre*, *Wnt1-Cre2;Confetti* mice exhibited robust labeling in CNC derivatives, including CGs and TH$^+$ neurons (Fig. 4, O and P). Analysis of PN7 *Wnt1-Cre2;Confetti* hearts identified a small number of large, coherent, single-colored myocardial clones within the RV, LV, and IVS myocardium and trabeculae (Fig. 4, O to Q). Immunophenotypic analysis indicated that these *Wnt1-Cre2;Confetti* ventricular clones were composed primarily of α-sarcomeric actinin$^+$ CMs and were occasionally paired with same-color TH$^+$ neurons (Fig. 4, O to Q). These findings conclusively demonstrate the common CNC developmental

origin of ventricular CMs and TH$^+$ neurons. Moreover, because of the very low clonal densities in *Wnt1-Cre2;Confetti* hearts, they also suggest that same-color TH$^+$ neuron-CM pairs likely indicate bipotency of CNC progenitors. However, because of the highly migratory phenotype of CNCs, alternative explanations, such as intermixing of CM-specific and neuron-specific CNC progenitor cell clones, cannot be entirely excluded.

Both the *Wnt1-Cre2;Confetti* and *Isl1-Cre;Confetti* hearts exhibited large, wedge-shaped, transmural myocardial clonal growth patterns, with a wide epicardial and a narrower endocardial side (Fig. 4, O to Q). This pattern of myocardial growth has been described before (*6*) and is consistent with the interpretation that each clone develops from a single fetal CNC progenitor that undergoes trabecular CM differentiation before expanding clonally during ventricular compaction and septation.

Another important observation from the fate-mapping experiments is that during fetal growth, *Isl1*$^+$ cells generate relatively few but massive and coherent, single-colored CM clones, whereas their contribution in TH$^+$ neurons is minimal (Fig. 4, K to Q). Conversely, in the postnatal heart, they generate relatively few but massive, single-colored TH$^+$ neural clones, whereas their CM contribution is minimal (Fig. 4, A to J). Accordingly, the observation that the number of CM or TH$^+$ clones remains relatively limited suggests that the amount of Isl1$^+$ cells that differentiate into CMs and TH$^+$ neurons, respectively, is limited, both in the fetal and the postnatal hearts. However, the observation that CNC-CM and CNC-TH$^+$ clones expand in size only before and after birth, respectively, suggests that transition to the postnatal life produces signals that inhibit CNC-CM proliferation in favor of CNC-TH$^+$ clonal expansion. Notably, zebrafish hearts do not exhibit this postnatal CNC-CM proliferation deficit, and loss of adult CNC-CMs has been recently shown to be sufficient to inhibit adult heart regeneration in this highly regenerative animal model (*13*).

Thus, on the basis of the *Isl1-MCM* fate-mapping and *Confetti* clonal experiments, we conclude that Isl1$^+$ CNCs have the capacity to generate both trabecular CMs and TH$^+$ neurons. Moreover, we conclude that fetal CNC-CMs exhibit high clonal expansion capacity and can undergo multiple cell divisions as indicated by the large *Confetti* clones, but this property is lost upon transition to the postnatal life.

Reconstruction of postnatal Isl1$^+$ CNC differentiation trajectory through scRNAseq

To further challenge the interpretation that postnatal Isl1$^+$ CNCs contribute to the Nkx2-5$^+$ CM lineage, the *Isl1*$^+$ and *Nkx2-5*$^+$ fractions were subselected from the scRNAseq datasets and subjected to pseudotime trajectory reconstruction through unsupervised, machine-learning approaches (*26*) (Fig. 5A). Overall, there were 442 *Isl1*$^+$, 385 *Nkx2-5*$^+$, and 41 *Isl1*$^+$/*Nkx2-5*$^+$ scRNAseq profiles that, when computed in 10 dimensions, were constructed into a principal graph with three branch points leading to six distinct cell states [(Fig. 5, B and C). Branch point 1 diverges into cell state 2 (CS2), CS3, and CS4. Branch point 2 leads to CS5 and to branch point 3, which subsequently bifurcates into CS1 and CS6 (Fig. 5B). Each state represents transcriptionally similar scRNAseq profiles, whereas the length of its trajectory projects the amount of transcriptional change as progress in pseudotime (*26*). Cluster-based analysis delineated that the 868 cells of the *Isl1*$^+$/*Nkx2-5*$^+$ trajectory represent 14 of the 15 UMAP clusters, with the macrophages (cluster 13) as the only exception (Fig. 5D and fig. S9A). The myocardial clusters (10 and 14) are ordered at the end of the CS4 trajectory (Fig. 5D and fig. S9A), and therefore, CS4 is classified as the myocardial lineage trajectory. CS4 branches out of branch point 1, which is the point at which CS3 bifurcates into the myocardial and nonmyocardial (CS1, CS2, CS5, and CS6) trajectories (Fig. 5B). Therefore, we classified CS3 as the root state.

Expression of *Isl1* and *Nkx2-5* showed minimal overlap within the reconstructed trajectories with only 41 of the 868 cells coexpressing the two genes (Fig. 5C). Of these 41 coexpressors, 4 were in the myocardial trajectory, 2 at the root cell state, and 35 in nonmyocardial trajectories (Fig. 5C). Moreover, 40 of the 41 *Isl1*$^+$/*Nkx2-5*$^+$ cells were of ventral identity (Fig. 5C), which, as shown earlier (i.e., Fig. 3), indicates that Isl1 is translationally silenced in these cells. This agrees with previous observations that Isl1 and Nkx2-5 suppress each other during cardiac differentiation (*1*). Notably, consistent with our previous findings (*10*), a small fraction of *Isl1*$^+$ cells (27 of 483) and *Nkx2-5*$^+$ cells (5 of 426) coexpressed the proto-oncogene *Kit*.

From the 14 UMAP clusters in the *Isl1*$^+$/*Nkx2-5*$^+$ pseudotime trajectories, only 5 clusters—7 (CNCs), 9 (venous endothelial), 10 (working CMs), 11 (low-quality/dying CMs), and 14 (Gja5$^+$ conduction system CMs)—follow the myocardial lineage trajectory (CS4) (Fig. 5D and fig. S6, A and B). Specifically, the myocardial cells (clusters 10 and 14, as well as the low-quality cluster 11) are ordered at the end of the trajectory, consistent with their terminal differentiation state (fig. S6, A and B), whereas *Isl1*$^+$ CNCs are placed at the start of the trajectory resembling a progenitor state (fig. S6, A and B). All, except one, *Isl1*$^+$ CNC profiles are of IFT/dorsal identity (fig. S6C), indicating functional Isl1 protein expression. Similarly, the single *Isl1*$^+$ cell from the endothelial cluster that is placed in the myocardial trajectory is also of IFT/dorsal identity (fig. S6C), thereby excluding an OFT/aSHF CPC origin. To investigate further whether any of the postnatal Isl1$^+$ cells represent aSHF-CPCs, we also analyzed the *Isl1*$^+$/*Nkx2-5*$^+$ trajectory on the basis of *Kdr* and *Pdgfra* expression. These two receptors are transiently coexpressed on the surface of most multipotent cardiogenic mesoderm CPCs, including aSHF, during mouse and human development (*1*, *3*). Overall, there were 415 *Pdgfra*$^+$, 10 *Kdr*$^+$, and 4 *Kdr*$^+$/*Pdgfra*$^+$ cells (fig. S6D). However, the *Kdr*$^+$/*Pdgfra*$^+$ was of IFT/dorsal cell origin and belonged to UMAP clusters 1, 3, and 9, which are ordered at the end of the nonmyocardial trajectory CS1 (fig. S6D).

Thus, the above scRNAseq findings provide additional evidence that a subset of IFT/dorsal *Isl1*$^+$ CNC–derived cells in the postnatal mouse heart are endowed with CM differentiation capacity and contribute to the Nkx2-5$^+$ CM lineage. In contrast, we could not find any evidence supporting the presence of arterial pole/aSHF-derived postnatal CPCs.

Disruption of Wnt/β-catenin–Isl1 feedback loop promotes CNC-CM differentiation

To identify potential molecular mechanisms controlling the fate of postnatal *Isl1*$^+$ CPCs, we performed DEG analysis (*26*) on branch point 1, where the root state bifurcates toward myocardial or nonmyocardial trajectories (Fig. 5B and fig. S6A). There were 1924 branch-dependent DEGs (q value of <0.01) that were hierarchically clustered on a multiway heatmap into six gene modules. Each gene module indicates similar pseudotime trajectory–dependent expression patterns (Fig. 5E and data S1C). Gene modules 1 and 2 exhibit up-regulation in cell fate 2 and down-regulation in cell fate 1 genes.

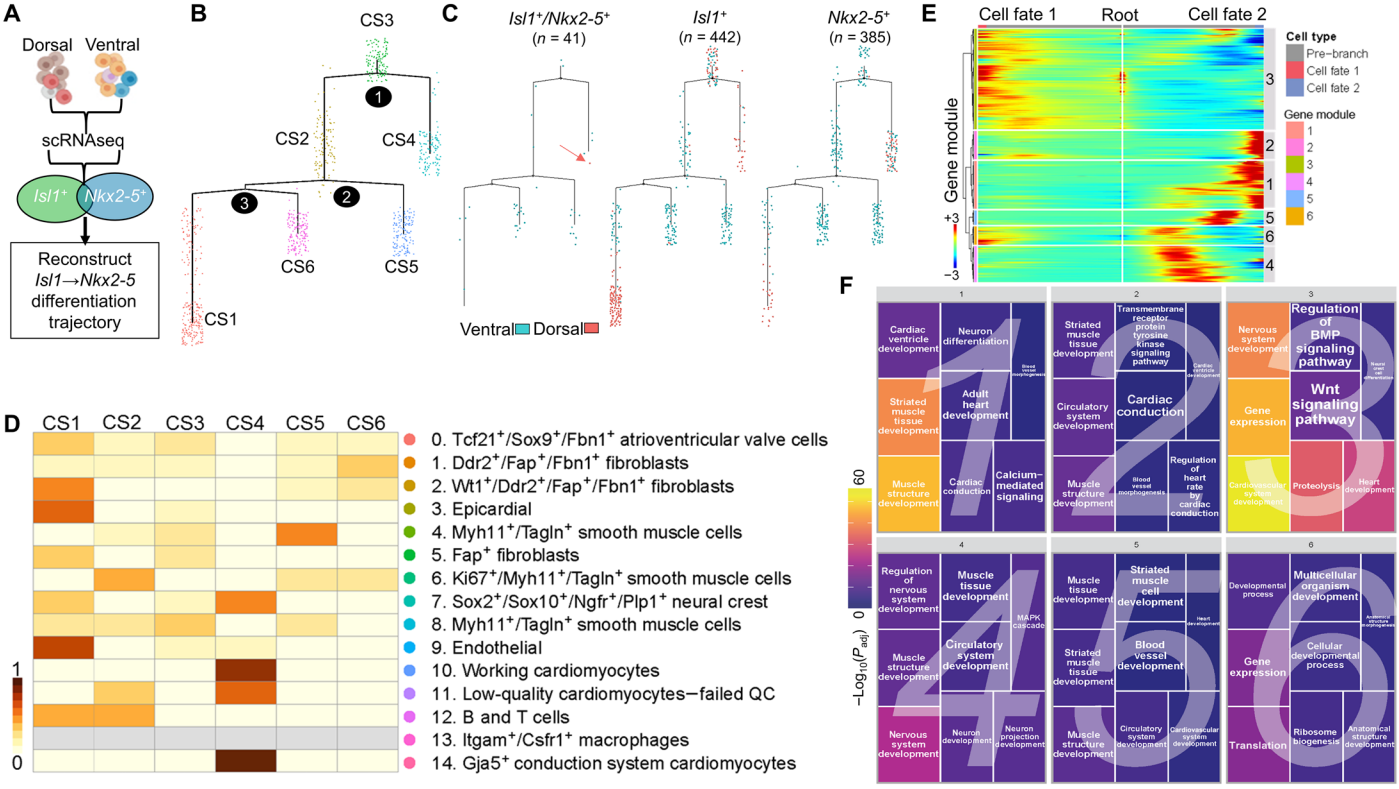

Fig. 5. Reconstruction of postnatal *Isl1*$^+$ and *Nkx2-5*$^+$ differentiation trajectories. (**A**) Experimental outline. (**B**) Ordering of the *Isl1*$^+$ and *Nkx2-5*$^+$ scRNAseq subsets ($n = 868$ cells) on the reconstructed trajectory. The trajectory has three branch points (black circles) leading into six different cell states (CS; color coded). CS3 is classified as the root; CS4 as the myocardial; and CS1, CS2, CS5, and CS6 as nonmyocardial states. (**C**) Ordering of the *Isl1*$^+$, *Nkx2-5*$^+$, and *Isl1*$^+$/*Nkx2-5*$^+$ subsets, based on dorsoventral identity. Arrow points to the only *Isl1*$^+$/*Nkx2-5*$^+$ dorsal cell. (**D**) Heatmap illustrating the distribution of UMAP clusters across cell states. CS4 is composed of clusters 7, 9, 10, 11, and 14. (**E**) Multiway heatmap of branch point 1–dependent DEGs (false discovery rate–adjusted $P < 0.01$), hierarchically clustered into six gene modules. Modules 1 and 2 correspond to the myocardial trajectory (CS4; cell fate 2), module 3 to the root (CS3), and modules 4 to 6 to nonmyocardial trajectories (cell fate 1). (**F**) Functional enrichment analysis of gene modules (false discovery rate–adjusted $P < 0.01$), visualized in a geometric treemap plot. Numbers 1 to 6 indicate gene modules. The scale of $-\log_{10}(P_{adj})$ values is both geometrically and color coded. Branched trajectories are plotted as a two-dimensional tree layout. MAPK, mitogen-activated protein kinase.

Gene module 3 exhibits up-regulation in root state (center) and cell fate 1 prebranch genes but down-regulation in cell fate 2 genes, whereas gene modules 4, 5, and 6 exhibit up-regulation in cell fate 2 prebranch genes (Fig. 5E). Functional enrichment analysis indicated that gene modules 1 and 2 are enriched in biological processes related to the myocardial lineage, including embryonic and adult heart development, heart contraction, cardiac conduction, and cardiac ventricle morphogenesis (Fig. 5F and data S2, C and D). Gene modules 4, 5, and 6 are more heterogeneous as indicated by their enrichment in prebranch genes related to myocardial, neuronal, and vascular biological processes (Fig. 5F and data S2, F to H), whereas gene module 3 is enriched in biological processes related to the cardiac and neural crest differentiation and proliferation, as well as proteolysis, gene regulation, and Wnt and bone morphogenetic protein (BMP) signaling pathways (Fig. 5F and data S2E). Thus, on the basis of the above pseudotime trajectory–dependent expression profiles and functional enrichment analyses, we conclude that gene module 3 captures the root state gene signature underlying the decisions of postnatal *Isl1*$^+$ cells toward myocardial or nonmyocardial fates, gene modules 1 and 2 capture the terminally differentiated CM states, and gene modules 4 to 6 capture the remaining cell states.

On the basis of scRNAseq functional enrichment analysis, the root state (gene module 3) of the *Isl1*$^+$/*Nkx2-5*$^+$ trajectory receives input from the Wnt and BMP signaling pathways (Fig. 5F and data S2E). During normal heart development, canonical Wnt signaling directly activates *Isl1* to inhibit CM differentiation and promote the expansion of aSHF CPCs, whereas repression of Wnt by canonical BMP signaling is required for down-regulation of *Isl1* and induction of cardiomyogenesis (*3*). Therefore, we sought to functionally test the role of canonical Wnt signaling in the fate of *Isl1*$^+$ CNCs. First, we genetically fate-mapped CNCs in the presence or absence of a Wnt/β-catenin gain-of-function (GOF) mutation, introduced through a previously described *Wnt1/GAL4/Cre-11* transgene (*27*). Consistent with the *Confetti*- and scRNAseq-based findings, CNCs under normal Wnt signaling contributed to all expected derivatives in the OFT and cardiac autonomic nervous system, as well as to Nkx2-5$^+$ CMs within the trabeculated (fig. S7A) and compact LV, RV, and IVS myocardium (fig. S7B). However, ectopic activation of *Wnt* produced a ~147-fold reduction in CM differentiation, while OFT and neuronal contributions were unaffected (fig. S7, C and D) (0.07 ± 0.04% versus 9.76 ± 0.77% myocardial labeling under the *Wnt1/GAL4/Cre-11* and *Wnt1-Cre2* drivers, respectively; $P < 0.0001$).

To better explore the effects of Wnt signaling on CNC cardiomyogenesis, we generated *Wnt1/GAL4/Cre-11;tdTomato* induced pluripotent stem cells (iPSC$^{Wnt1\text{-}GOF}$) and differentiated them into CNCs (fig. S7E) (*10*, *28*). Specification of iPSC$^{Wnt1\text{-}GOF}$ into Isl1$^+$ CNCs commences within 9 days of embryoid body (EB) differentiation, as indicated by induction of tdTomato; activation of *Wnt1*, *Isl1*, and *Nkx2-5* mRNAs; and colocalization of tdTomato with Isl1 (fig. S7, F and G). By day 12, tdTomato is expressed in 61.81 ± 5.76% EBs. Treatment of day 9 EBs with the glycogen synthase kinase-3 inhibitor CHIR99021 or DMSO did not promote cardiac differentiation, as indicated by the lack of spontaneously beating tdTomato$^+$ cells (fig. S7, H and I). In contrast, antagonism of Wnt with the tankyrase inhibitor XAV939 resulted in an ~86-fold increase in the emergence of spontaneously beating tdTomato$^+$/Nkx2-5$^+$ cells ($P < 0.0001$) (fig. S7, H to J). Notably, XAV939-mediated induction of Nkx2-5 was accompanied by down-regulation of Isl1 immunoreactivity (fig. S7J), supporting the scRNAseq *Isl1*$^+$/*Nkx2-5*$^+$ trajectory that Isl1 expression is silenced in Nkx2-5$^+$ cells (Fig. 5B and fig. S6, A and B).

Last, we conditionally deleted *Isl1* from CNCs (*Isl1-cKO*) by introducing an *Isl1*$^{Fl/Fl}$ allele to *Wnt1-Cre2;tdTomato* and *Wnt1/GAL4/Cre-11;tdTomato* mice (Fig. 6A). *Wnt1-Cre2;tdTomato;Isl1*$^{Fl/+}$ mutants are produced at the expected Mendelian ratios with grossly normal hearts, whereas *Wnt1-Cre2;tdTomato;Isl1*$^{Fl/Fl}$ embryos succumb to death between E14.5 and E15.5 (Fig. 6B). Analysis at E14.5 showed that, compared to their heterozygous littermates, *Isl1-cKO* mutant hearts exhibit increased concentration of tdTomato$^+$ CNCs in the atrioventricular (AV) cushions and abnormal RV and LV trabecular networks, including a marked reduction in the contribution of tdTomato$^+$ CNCs into Nkx2-5$^+$ trabecular and IVS CMs as well as muscular IVS defects (Fig. 6, C to E). Loss of *Isl1* under ectopic Wnt activity from the *Wnt1/GAL4/Cre-11* driver (*Isl1-cKO;Wnt1-GOF*) results in normal Mendelian genotypic ratios (Fig. 6B), but *Isl1-cKO;Wnt1-GOF* hearts exhibit a near-complete loss of tdTomato$^+$ sympathetic nerves and CMs and die shortly after birth as previously reported (*29*). However, in both *Wnt1-Cre2* and *Wnt1/GAL4/Cre-11* mice, heterozygous deletion of *Isl1* was accompanied by increased differentiation of CNCs into tdTomato$^+$ myocardium compared to *Isl1*$^{+/+}$ controls (Fig. 6, F to H), indicating that, similar to its function in other neural crest derivatives (*30*), *Isl1* gene dosage influences the specification of CNCs toward CM versus non-CM fates. Therefore, on the basis of the above findings, we conclude that the IFT/dorsal Isl1$^+$ CNCs play an important developmental role in myocardial trabeculation, compaction, and sympathetic innervation and suggest that their fate is regulated through a forward reinforcing loop between Isl1 and Wnt/β-catenin signaling since ectopic Wnt signaling can partially rescue the Isl1-cKO phenotype.

DISCUSSION

The main finding of our study is that we have identified an Isl1$^+$ neural crest program in the IFT region that contributes a small number of highly proliferative trabecular CMs during mammalian cardiac chamber morphogenesis. We further found that this dorsal Isl1$^+$ neural crest program is sustained throughout postnatal heart growth but with diminished CM clonal expansion capabilities. We have arrived at this conclusion through a series of complementary experimental approaches, including traditional genetic lineage-tracing, iPSC-modeling, and scRNAseq experiments.

In keeping with our findings, previous studies provided evidence that silencing of heart field–specific Isl1 expression starts as early as E8.5 in mice. In particular, aSHF enhancer–specific β-galactosidase reporters were shown to exhibit broader expression than the endogenous Isl1 protein at the looped heart stage. However, this discrepancy has been heretofore attributed to the longer β-galactosidase half-life (*4*, *31*). We now show that, in fact, it is an indicator of Isl1 protein degradation due to the developmental activation of the ubiquitin-proteasome pathway, selectively in the OFT but not IFT region. A similar mechanism has been shown to regulate Isl1 protein levels in aSHF-CPCs at the crescent and linear heart tube stages (*24*). Here, we expand upon these findings by showing through lineage-tracing experiments that OFT-specific Isl1 degradation affects all Isl1-expressing cell types, regardless of their embryonic origin and identity (including SHF and CNC derivatives), indicating that this posttranslational mechanism is specific to the OFT domain rather than the lineage or type of cells. Notably, expression of *Isl1* is also silenced through the miRNA 17 to 92 cluster during aSHF-CPC differentiation (*23*). However, in our study, conditional deletion of *Dicer* was not sufficient to drive protein expression in ventral postnatal *Isl1*$^+$ cells, suggesting that this miRNA mechanism is restricted to aSHF enhancer–specific *Isl1* gene products during the early CM differentiation stages of aSHF-CPCs.

The permanent, developmental silencing of the Isl1$^+$ OFT domain is further supported by previous studies showing that the activity of cardiac mesoderm–specific enhancers diminishes before E12.5 in mice (*5*). However, at first glance, this finding seems somewhat contradictory to ours, because we show that developmental silencing of Isl1 is primarily posttranslational rather than transcriptional. We show that *Isl1-nLacZ* and *Isl1* mRNAs continue to be abundantly expressed in both heart field (SHF/SAN) and CNC derivatives throughout development and that transcriptional silencing of *Isl1* occurs after birth through a relatively slow process, which takes months to complete and involves dorsoventral differences in postnatal PRC2 activity. We further show that postnatal *Isl1* silencing occurs in a regionalized fashion, selectively in the OFT but not IFT domain, and affects SHF and CNC derivatives equally. However, compared to Kappen *et al.* (*5*), we used an *Isl1-nLacZ* knock-in that exhibits broad activity from both the neural- and heart-specific regulatory elements. Therefore, the seemingly discrepant findings likely indicate that *Isl1* expression is sustained in the fetal and postnatal heart through non-aSHF elements. This explanation is further supported by the ChIP-seq analysis indicating H3K27me3 silencing of the heart field–specific but not the neural *Isl1* regulatory elements (fig. S6).

Previous studies in chick embryos show that CNCs entering through the venous pole are apoptosis prone (*7*), raising the possibility that the decrease in postnatal OFT *Isl1-nLacZ* activity reported in our study could also be partially explained by apoptotic cell death. However, our scRNAseq studies suggest that the degree to which postnatal OFT Isl1$^+$ cells undergo apoptosis is likely negligible. Several explanations may account for the differences between our study and that of Poelmann and Gittenberger-de Groot (*7*). First, Poelmann and Gittenberger-de Groot (*7*) studied CNC development in bird embryos, whereas our study focuses in the postnatal mouse heart. Second, Poelmann and Gittenberger-de Groot (*7*) observed the induction of apoptosis in IFT CNCs, whereas our study notes the loss of *Isl1-nLacZ* expression in the OFT. Third, compared to Poelmann and Gittenberger-de Groot (*7*), our lineage-tracing findings indicate that loss

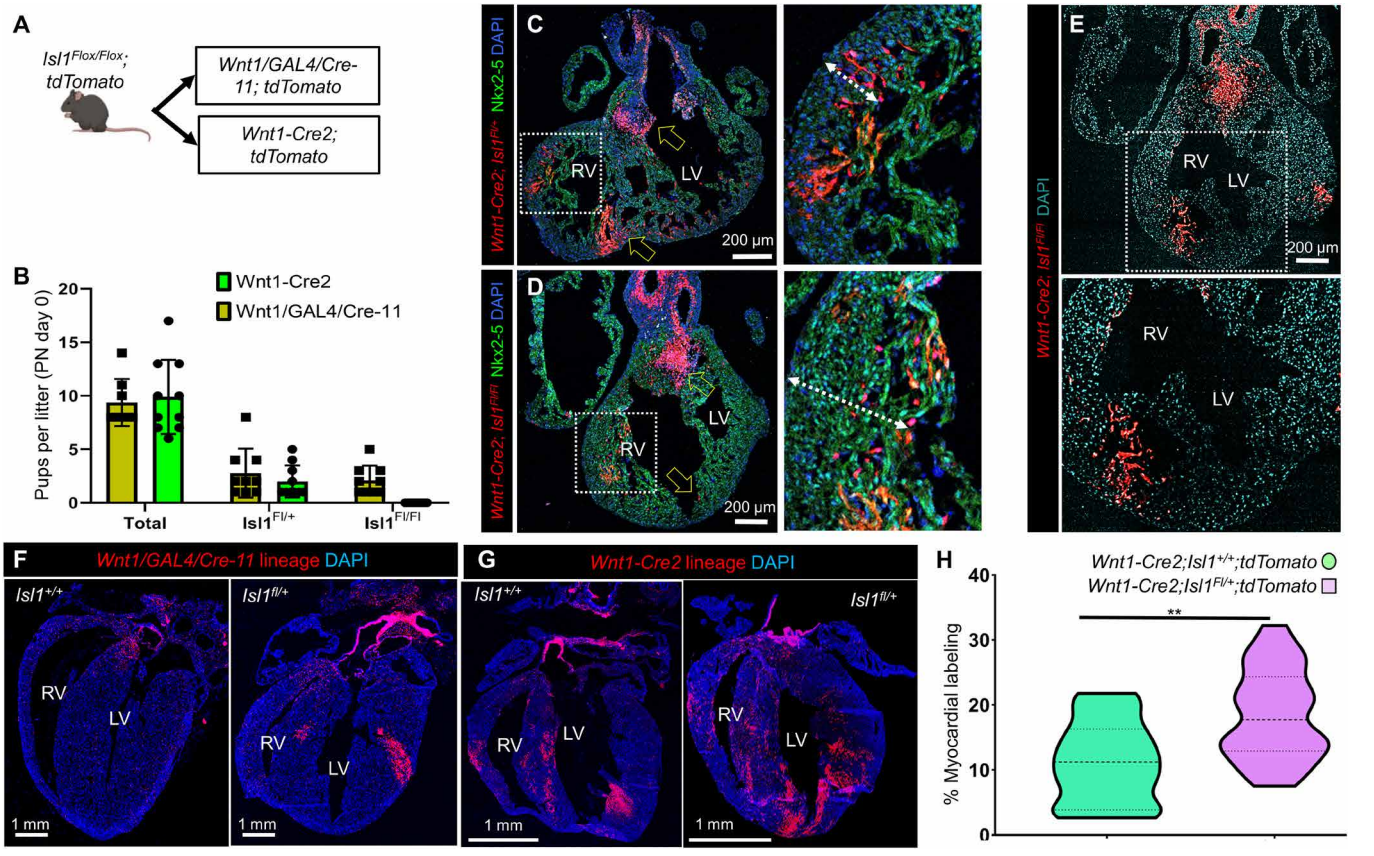

Fig. 6. *Isl1* gene dosage regulates the cardiomyogenic fate of CNCs. (**A**) Experimental outline. (**B**) Pup survival per litter following conditional deletion of *Isl1* in CNCs by *Wnt1-Cre2* ($n = 43$ pups) and *Wnt1/GAL4/Cre-11* ($n = 74$ pups). CNC-specific Isl1-cKO is developmentally lethal but is rescued by ectopic Wnt. (**C** and **D**) Expression of tdTomato in E14.5 *Wnt1-Cre2;tdTomato;Isl1*$^{Fl/Fl}$ and *Wnt1-Cre2;tdTomato;Isl1*$^{Fl/+}$ hearts. *Isl1-cKO* hearts exhibit abnormal migration of CNCs into the ventricles and endocardial cushions (open arrows). Left panels are higher-magnification images of boxed areas. Note the thickened myocardial wall (arrows) and abnormal trabeculations in *Isl1-cKO* heart compared to the littermate control. (**E**) Muscular ventricular septal defect in an *Isl1-cKO* heart. (**F** and **G**) Expression of tdTomato in *Isl1*$^{+/+}$ and *Isl1*$^{Fl/+}$ postnatal hearts under the *Wnt1-Cre2* and *Wnt1/GAL4/Cre-11*. Loss of myocardial derivatives by ectopic Wnt through *Wnt1/Gal4/Cre-11* is partially rescued when the *Isl1* gene dosage is reduced to half (E). Similarly, a reduction of Isl1 gene dosage by half promotes an increase in CNC-CM differentiation by 66% in *Wnt1-Cre2* mice (F). (**H**) Violin plot of *Wnt1-Cre2* myocardial labeling as a percentage of the total area of the heart, between *Isl1*$^{+/+}$ and *Isl1*$^{Fl/+}$ ($n = 3$ mice per group, four to five slides per heart, ***$P = 0.0022$, paired *t* test). Values are means ± SEM.

of OFT *Isl1-nLacZ* expression is not CNC specific but affects all *Isl1*$^{+}$ cardiac lineages. Last, because unlike the loss of Isl1 protein and *Isl1-nLacZ* expression, we have not observed any age-dependent dilution in the expression of reporter genes in *Isl1-Cre* or *Isl1-MCM* postnatal OFTs, indicating that cell death does not contribute substantially to the loss of Isl1 protein and *Isl1-nLacZ* expression in the postnatal mouse OFT.

Differentiation of CNCs to CMs has been previously shown in zebrafish (*11*–*13*) and mice (*10*, *11*). Developmentally, CNCs primarily contribute trabecular CMs in both species, whereas in mice, they further contribute IVS CMs, a structure that has not evolved in the univentricular zebrafish heart (*10*–*12*). Consistently, we show that migration and CM differentiation are compromised in Isl1-cKO CNCs and that these mice die at midgestation with abnormalities in AV cushions, IVS, and trabecular myocardium. Previous studies in mouse embryos have shown that IVS and trabecular CMs are clonally related and that these fetal CM populations develop progressively, during E10.5 to PN7, as transmural, wedge-shaped clusters, with a wide epicardial and a narrower endocardial side (*6*). This description matches the CM clones produced from CNCs (e.g., Fig. 6). Moreover, *Confetti* analysis illustrated that these are primarily single-colored, coherent clones, which, as shown before (*6*), indicates that upon initial differentiation, fetal CNC-CMs go through a stage of massive proliferative expansion (e.g., Fig. 4, O to Q). The proliferative expansion capability of CNC-CMs has been shown to underlie adult heart regeneration in zebrafish (*13*), but our findings indicate that this property is lost in the postembryonic mouse heart, suggesting that its therapeutic reactivation could possibly enhance the adult heart regenerative capabilities in mammals.

Our *Confetti* fate-mapping experiments indicate that CNC-CMs lose their clonal expansion capabilities in the postnatal heart. This could be due to loss of clonal expansion signals in the cells' microenvironment and due to intrinsic cell changes. A potential clonal expansion mechanism that is deregulated at birth involves the postnatal changes in cardiac metabolism. Specifically, during fetal growth, trabecular CMs are thought to proliferatively expand by undergoing a transient metabolic switch from mitochondrial respiration to anaerobic glycolysis (*32*). A similar mechanism has been implicated in heart regeneration in neonatal mice, as well as in zebrafish heart

development and postnatal regeneration (*17*, *33*). A recent study identified a small group of Sox10$^+$ CMs within the developing and adult zebrafish heart, which exhibit a distinct metabolic profile and are essential for adult zebrafish heart regeneration (*13*). At the molecular level, it has been shown that this metabolic switch is regulated through oxygen tension and the hypoxia-inducible factor 1α in mice and Neuregulin/ErbB2 signaling in zebrafish (*17*, *32*, *33*). Thus, it would be interesting to examine whether these signaling pathways can be therapeutically modulated to revoke clonal expansion capabilities in postnatal CNC-CMs and, consequently, heart regeneration in adult mammals.

We further show that mice with heterozygous loss of *Isl1* in CNCs develop normally but exhibit a significant increase in the number of Nkx2-5$^+$ CNC-CM clones (e.g., Fig. 6, G and H). This intriguing observation suggests that *Isl1* gene dosage influences the CM versus non-CM fates of CNCs and is reminiscent of the role of *Isl1* in specifying motor neuron versus V2a interneuron identities in the neural tube (*30*). In particular, Song *et al.* (*30*) showed that heterozygous loss of *Isl1* resulted in higher Lhx3 and Nkx6.1 levels, which consequently altered the relative stoichiometries of the Ldb1/Lhx3/Isl1 complexes in favor of V2a interneurons versus motor neuron differentiation. Similarly, formation of Ldb1/Isl1 complexes were recently shown to regulate Isl1 protein levels by controlling its proteasomal degradation during aSHF-CPC differentiation (*24*). Here, we were able to determine through scRNAseq and pharmacologic experiments that a similar mechanism contributes to the sustained expression of Isl1 in dorsal CNCs. Last, as predicted through scRNAseq-based lineage trajectory reconstruction, we further show that the CNC-CM fate is additionally regulated through a forward reinforcing loop between Wnt/β-catenin and Isl1. We show that mice with ectopic activation of Wnt in CNCs are viable and fertile but exhibit ~147-fold decrease in CNC-CMs. Impaired CM differentiation could be rescued by eliminating one of the *Isl1* alleles, as well as through pharmacologic inhibition of Wnt in iPSC-derived Isl1$^+$ CNCs. Notably, the grossly normal cardiovascular phenotype of Wnt1-GOF mice suggests that CNC-CMs are not essential for the development of trabeculated and IVS myocardium since it appears to be compensated through other CM sources. Loss of CNC-CMs in zebrafish does not affect heart development or final CM numbers but leads to pathologic CM hypertrophy (*12*) and impaired postnatal cardiac regenerative capacity (*11*, *13*). We have also observed signs of LV and IVS hypertrophy in Wnt1-GOF mice (e.g., Fig. 6, F to H); however, whether this is normal or pathological was not examined in this study.

There are also some potential limitations in our study that should be noted. For example, our finding that the dorsal Isl1$^+$ population is CNC derived is in agreement with previous work (*14*, *22*, *34*) and is based on lineage-tracing experiments with the *Wnt1-Cre2* mouse line—one of the best characterized, mammalian neural crest–specific animal models. However, because this specific Cre/loxP line is not temporally inducible, it is possible that recombination might have occurred postnatally from residual *Wnt1* expression in non-CNC Isl1$^+$ cells. This could have been potentially resolved through a temporally controlled *Wnt1-Cre* mouse line. However, the *Wnt1* regulatory elements driving *Cre* expression are transiently activated during CNC development, and therefore, *Wnt1* is not a suitable marker for temporally targeting CNCs in the postembryonic heart. Furthermore, to our knowledge, there are currently no known genetic markers that can reliably target CNCs after embryonic development. Fortunately, however, the possibility of ectopic Cre expression in our postnatal *Wnt1-Cre2* studies is minimal because, based on our scRNAseq analysis, expression of *Wnt1* is undetectable in postnatal *Isl1*$^+$ cells (Fig. 1C).

Similarly, the *Isl1-MCM* genetic lineage-tracing experiments demonstrate unequivocally the differentiation of postnatal *Isl1*$^+$ cells into CMs and therefore depart from the current interpretation that non-CMs do not contribute any CMs in the neonatal heart (*15*). However, because the *Isl1-MCM* allele is not CNC specific, the possibility that some of the postnatal Isl1$^+$ cells from which *Isl1-MCM* CMs arise are not CNCs, but SHF remnants as previously suggested (*16*), cannot be entirely excluded. A potential solution to this question could have been the use of the *Confetti* reporter under the control of the *Isl1-MCM*. However, in our hands, the *Isl1-MCM* and *Isl1-Cre* mouse lines are not sufficiently strong to fully recombine the *Confetti* reporter in CNCs. Therefore, this approach warrants the development of new, higher-resolution experimental tools.

To address the limitations described above, we validated the in vivo lineage-tracing experiments through an orthogonal, unbiased scRNAseq-based approach. Accordingly, scRNAseq-based lineage trajectory reconstruction of postnatal *Isl1*$^+$ cells recapitulated our postnatal lineage-tracing findings and delineated the relationship of postnatal *Isl1*$^+$ cardioblasts to dorsal CNCs rather than SHF (or other) lineages. However, as with any experimental system, this approach has its own limitations. For example, a potential caveat in our experimental design is that, following enzymatic dissociation, cells were recovered in culture for 5 days before scRNAseq. This may have produced culture-induced alterations in single-cell gene expression profiles compared to in situ conditions. However, on the basis of our data, we propose that this experimental design is suitable compared to freshly dissociated single-cell methods, for several reasons. First, compared to other tissue types, the heart is highly fibrous and therefore requires relatively harsh and lengthy enzymatic dissociation conditions that could markedly affect the integrity of the isolated cells and introduce dissociation-induced gene expression artifacts (*35*); second, similar approaches involving tissue culture recovery of primary cells for up to 7 days before scRNAseq have been used before for the discovery of rare cell types in other tissues (*36*); and third, we have shown before that postnatal Isl1$^+$ OFT cells from *Isl1-nLacZ* mice can be dissected and cultured for several weeks without notable changes in *LacZ* expression and phenotype (*28*). Last, the fidelity of our experimental approach can be appreciated when compared to two recent scRNAseq studies. In the first study, scRNAseq of 55,611 cells, freshly isolated from developing cardiac OFTs of CD1 mice, showed how expression of *Isl1*$^+$ is limited to a small portion of aSHF-derived arterial SMCs at the base of the large coronary arteries (*37*). However, several other *Isl1*$^+$ OFT cell types, which are identified in our scRNAseq study and orthogonally validated through genetic lineage-tracing experiments, were not reported, including the rare population of *Isl1*$^+$ CNC–derived SMCs and sympathetic nerves. In the second study, scRNAseq of 3717 single cells, freshly isolated from a 6.5- to 7-week-old postconception human embryonic heart, reported the expression of Isl1$^+$ exclusively in OFT CNCs (*38*). Compared to our study, this analysis also did not identify several *Isl1*$^+$ cell types, such as the Isl1$^+$ IFT CNCs, and the Isl1$^+$ aSHF and pSHF derivatives in the OFT, OFT base myocardium, and SAN were not reported. Thus, despite the limitations described above, our scRNAseq data closely recapitulate the in vivo conditions.

In summary, our analysis provides evidence that the postembryonic murine heart sustains a limited number of organ-founding CNCs in the IFT region that retain their ability to generate de novo CMs after birth but lose their CNC-CM clonal expansion properties. Therefore, we propose that the loss of regenerative capabilities in the postnatal mammalian heart may not be directly related to the limited CM differentiation capacity as currently thought (*15*) but mostly to the loss of CNC-CM clonal expansion signals. Furthermore, our findings point to ventricular trabeculation and compaction as a key developmental stage for identifying CNC-CM proliferation signals that could be revoked in the postembryonic heart for regenerative purposes.

MATERIALS AND METHODS

Mice

All animals were maintained in an American Association for Accreditation of Laboratory Animal Care (AAALAC)–approved animal facility at the University of Miami, Miller School of Medicine, and procedures were performed using Institutional Animal Care and Use Committee–approved protocols according to National Institutes of Health (NIH) standards. The *Isl1-nLacZ* mice have been described before (*14*). The *IRG* (stock no. 008705), *tdTomato* (stock no. 007914), *Confetti* (stock no. 017492), *Wnt1-Cre2* (stock no. 022501), *Isl1-MerCreMer* (stock no. 029566), *Isl1*$^{fl/fl}$ (stock no. 028501), *Dicer*$^{fl/fl}$ (stock no. 006366), *Isl1-Cre* (stock no. 024242), and *Wnt1/GAL4/Cre-11* (stock no. 003829) mice were obtained from the Jackson laboratory. The *Mef2c-AHF-Cre* mice were cryorecovered at the University of Miami, Sylvester Comprehensive Cancer Center's Transgenic animal facility, from material obtained from the Mutant Mouse Regional Resource Centers (MMRRC, strain ID: 30262). The *Wnt1-Cre2* mice were bred through the female germ line. The *Mef2c-AHF-Cre* mice were bred through the male germ line. Genotyping was performed by an independent provider via an automated real-time PCR system (Transnetyx). All analyses were performed in age-matched males and female littermates from multiple litters.

Human fetal heart tissue

Human fetal heart tissues (15 to 22 weeks of gestation) were obtained from authorized sources (Advanced Bioscience Resources Inc., Alameda, CA) following Institutional Review Board approval. Upon arrival, tissues were fixed in 10% buffered formalin for ~24 hours, embedded in paraffin, and cut into 4- to 5-μm-thick sections.

Tamoxifen injection

For *Isl1-MerCreMer* recombination, 2-day-old neonatal mice were injected subcutaneously with 50 μl of tamoxifen (Sigma-Aldrich), dissolved in peanut oil (Sigma-Aldrich) at a concentration of 20 mg/ml, as previously described (*10*). Animals were euthanized 48 hours later. For fate-mapping experiments, tamoxifen injections were repeated on days 2 and 4, and animals were euthanized 2 weeks later. For Dicer-cKO experiments, injections were repeated on days 2, 4, and 6, and animals were euthanized on day 7.

Immunohistochemistry and immunocytochemistry

For immunocytochemical analysis, cells were fixed in 4% paraformaldehyde, blocked for 1 hour with 10% normal donkey serum, and processed for immunostaining as described before (*10*). Immunofluorescence analysis of mouse heart tissues was performed in 10-μm-thick cryosections. Immunofluorescence analysis of human fetal heart samples was performed in 4- to 5-μm-thick formalin-fixed, paraffin-embedded tissue sections. Antigen unmasking was performed by microwaving the slides for 2 × 10 min in citrate buffer solution (pH 6) (Thermo Fisher Scientific). Sections were then blocked for 1 hour at room temperature with 10% normal donkey serum (Chemicon International Inc., Temecula, CA), followed by overnight incubation at 4°C with the primary antibody.

The following primary antibodies were used for immunohistochemistry: EGFP (enhanced green fluorescent protein; 1:500; Aves, #GFP-1020); H3K27me3 (1:200; Millipore Sigma-Aldrich, #07-449); HCN4 (1:40; Alomone, #APC052); sm22a (1:500; Abcam, #ab14106); anti-sarcomeric α-actinin (1:100; Abcam, #ab9465); TH (1:500; Novus Biologicals, #NB300); Isl1 (1:1000; ab109517, Abcam; or a mixture of 1:10 of #40.2D6 and 1:100 of #39.4D5, Developmental Studies Hybridoma Bank); cardiac myosin light chain-2 (1:200; Novus Biologicals, NBP1-40754); Nkx2.5 (1:50; Santa Cruz Biotechnology, #SC8697) and cardiac troponin-T (1:200; Abcam, ab8295); and Neurofilament M (1:200; Abcam, #7794). Subsequently, the antibodies were visualized by incubating the sections for 1 hour at 37°C with fluorescein isothiocyanate; Cy3- and Cy5-conjugated F(ab′)2 fragments of affinity-purified secondary antibodies (1:200; Jackson ImmunoResearch); or Alexa Fluor 488, Alexa Fluor 568, and Alexa Fluor 633 dyes (1:500; Thermo Fisher Scientific).

Western blot

Protein lysates were prepared in radioimmunoprecipitation assay buffer and quantified with the Bradford assay (Bio-Rad). Electrophoresis was performed in precast, NuPage 4 to 12% bis-tris protein gels before transferring into polyvinylidene difluoride membranes using the Trans-Blot Turbo transfer system (Bio-Rad). Before blocking and antibody incubation, membranes were stained with Ponceau S reagent (Sigma-Aldrich, #P3504) to visualize protein bands and cut at specific sizes so different antibodies could be tested at the same time. Western blots were performed using antibodies against H3K27me3 (0.4 μg/ml; Sigma-Aldrich, rabbit polyclonal), Isl1 (1:10,000; rabbit monoclonal, Abcam), Hsp90 (1:2000; rabbit polyclonal, Cell Signaling Technology), Gapdh (1:2000; rabbit monoclonal, Cell Signaling Technology), a goat anti-rabbit immunoglobulin G, and horseradish peroxidase–linked antibody (1:2000; Cell Signaling Technology). Densitometry analysis of Western blots was performed using Fiji ImageJ.

X-gal staining and quantification

X-gal staining was performed as previously described (*10*). Briefly, whole hearts were collected, washed in ice-cold Hanks' balanced salt solution, and fixed in 4% paraformaldehyde at 4°C for 30 min. Following fixation, samples were rinsed twice in ice-cold phosphate-buffered saline (PBS) and permeabilized overnight at 4°C, by shaking gently in wash solution (PBS, 0.02% sodium deoxycholate, and 0.01% IGEPAL). The next day, samples were transferred in staining solution [wash solution supplemented with 5 mM $K_3[Fe(CN)_6]$, 5 mM $K_4Fe(CN)_6{\cdot}3H_2O$, 2 mM $MgCl_2$, and x-gal (1 mg/ml)] and incubated overnight at 37°C, with gentle shaking. Samples were then washed in wash solution to remove any precipitation, fixed for 10 min in 2% paraformaldehyde, and imaged in a Zeiss Discovery.V8 stereomicroscope equipped with a Nikon D7200 digital camera. For x-gal quantification, whole-heart images in jpeg format and their respective x-gal$^+$ areas were selected in Adobe Photoshop Elements (version 12.1) using the semiautomated color-range selection tool and converted into pixel values. The amount of x-gal was

expressed as the percentage of x-gal$^+$ pixels per total pixels of the whole heart.

Quantification of myocardial contribution in Isl1$^{fl/fl}$, *Wnt1/GAL4/Cre-11*, and *Wnt1-Cre2* mice

Mouse hearts were fixed in 4% paraformaldehyde for 24 hours at 4°C, followed by overnight incubation in 30% sucrose, and embedded in optimal cutting temperature (OCT) compound (TissueTek), as previously described (*10*). Long-axis 10-μm-thick cryosections were prepared and immunostained for cardiac myosin light chain-2 (1:200; Novus Biologicals, NBP1-40754) followed by a Cy-5–conjugated donkey anti-rabbit secondary antibody, as previously described (*10*). Slides were mounted with fluoroshield mounting medium with 4′,6-diamidino-2-phenylindole (Abcam, #ab104139) and imaged on a Zeiss LSM 710 confocal microscope (Carl Zeiss MicroImaging Inc., Thornwood, NY), using the Zeiss ZEN software (version 2009, Carl Zeiss Imaging Solutions GmbH). For *Confetti*, samples were imaged in a Leica SP5 inverted microscope at the University of Miami Analytical Imaging Core Facility. To quantify the percentage of ventricular myocardium expressing *Cre* reporters, the areas of Cre$^+$/cmlc2$^+$ were quantified and expressed as a percentage of the total area of Cy-5$^+$ (cmlc2$^+$) myocardium per slide, using the ImageJ area analysis software. A total of two to five slides were analyzed per heart.

Quantitative PCR

Gene expression analysis was performed as described before (*10*). Briefly, following total RNA extraction with the RNeasy mini kit (Qiagen) and complementary DNA synthesis with the high-capacity reverse-transcription kit (Applied Biosystems), samples were subjected to quantitative PCR in an iQ5 real-time PCR detection system (Bio-Rad), using the TaqMan Universal Master mix (Applied Biosystems). The following probes were used: *Gapdh* (Mm99999915), *Isl1* (Mm00517585_m1), *Wnt1* (Mm01300555_g1), and *Nkx2-5* (Mm01309813_s1).

H3K27me3 and H3K27ac ChIP-seq analysis

The following publicly available datasets were obtained from the mouse ENCODE project (www.encodeproject.org): for H3K27me3 ChIP-seq mouse hearts: E10.5 (ENCSR266JQW), E14.5 (ENCFF129FZH), PN0 (ENCSR782DGO), and PN week 8 (ENCFF344SFV); for H3K27me3 ChIP-seq mouse hindbrain: E10.5 (ENCSR582S); for H3K27ac ChIP-seq mouse hearts: E10.5 (ENCS582SPN), E14.5 (ENCFF034YQZ), PN0 (ENCSR675HDX), and PN week 8 (ENCFF691YDA); and for H3K27ac ChIP-seq mouse hindbrain: E10.5 (ENCSR594JGI). The mouse *Isl1* enhancer and promoter regions were obtained from the University of California Santa Cruz (UCSC) Genome Browser database [UCSC Genome Browser on Mouse December 2011 (GRCm38/mm10) Assembly, http://genome.ucsc.edu]. For the analysis, fold-over-control signal tracks were used, depicting control-normalized tag density from two biological replicates per time point, pooled together.

Generation, characterization, and differentiation of iPSC$^{Wnt1\text{-}GOF}$

The iPSC$^{Wnt1\text{-}GOF}$ were generated from tdTomato-negative neonatal cardiac fibroblasts, derived from *Wnt1/GAL4/Cre-11;tdTomato* mice, using a polycistronic lentivirus (STEMCCA, Millipore) as previously described (*10*, *28*). iPSC$^{Wnt1\text{-}GOF}$ were propagated without feeders on 0.1% gelatin-coated plates (Millipore), with NDiff227 (Clontech), supplemented with leukemia inhibitory factor (1000 U/ml; Millipore), 1 μM PD0325901 (Tocris), and 3 μM CHIR99021 (Tocris). For CNC differentiation, iPSC$^{Wnt1\text{-}GOF}$ were trypsinized into single cells (Thermo Fisher Scientific), washed twice, and resuspended at a final concentration of 25,000 cells/ml in IMDM (Iscove's Modified Dulbecco's Medium), 2 mM L-glutamine, 20% fetal bovine serum (Thermo Fisher Scientific), 0.1 mM nonessential amino acids, and 0.1 mM β-mercaptoethanol (all from Thermo Fisher Scientific). EB differentiation was performed using the hanging-drop method, as previously described (*10*, *28*). During the first 48 hours of differentiation, EBs were supplemented with 2 μM dorsomorphin (Tocris) or DMSO. For canonical Wnt/β-catenin inactivation, EBs were supplemented with 1 μM XAV939 or DMSO on day 9 of differentiation. For canonical Wnt/β-catenin activation, EBs were supplemented with 3μM CHIR99021 or DMSO on day 9 of differentiation. All samples were cultured under 5% CO_2 atmosphere at 37°C. EBs were monitored daily for the emergence and quantification of tdTomato$^+$ beating cells in an Olympus IX81 fluorescence microscope as described before (*10*, *28*).

Isolation of primary cardiac cells for scRNAseq and in vitro pharmacologic experiments

For the scRNAseq and MG132 inhibitor experiments, 3-day-old *Isl1*$^{+/+}$ male and female neonatal mice were used (n = 15 for each experiment). Briefly, the cardiac apex and the dorsal and ventral domains of the cardiac base were dissected from each neonate and combined together to generate three pools of apical, dorsal, and ventral cardiac tissues, respectively. The ventral domain included the proximal Ao, PA, and OFT base. The dorsal domain included the SAN and CGs. Each pool was subsequently washed twice in D-PBS supplemented with 1% penicillin-streptomycin and minced into ~2-mm fragments as previously described (*10*, *28*). Samples were then washed again, resuspended in 3 ml of digestion buffer [Hanks' balanced salt solution, supplemented with collagenase type IV (2 mg/ml), dispase II (1.2 U/ml), and 1% penicillin/streptomycin), and incubated at 37°C for 15 min with gentle rocking. Digested samples were then gently triturated 10 to 20 times using a 10-ml serological pipette. This process was repeated three more times for a total digestion time of 45 min. Dissociated cells were then collected and washed two times with D-PBS, by centrifuging at 100*g* for 3 min. Last, the cell suspension was passed through a 40-μm nylon strainer, resuspended in plating medium (RPMI 1640, supplemented with 1% L-glutamine, 1% penicillin/streptomycin, and 2% B27 minus insulin), and seeded in 0.1% gelatin-coated 12-well or 24-well plates at a density of 100,000 cells/ml. Cells were fed with fresh plating medium every other day for a total of 5 days. For the MG132 experiments, 4 wells of a 24-well plate from each cell pool were cultured on day 5 with or without 25 μM MG132 for 90 min. For the scRNAseq experiment, 4 wells of a 24-well plate from the dorsal and ventral pools were dissociated on day 5 with TrypLE (Thermo Fisher Scientific), passed through a 40-μm nylon strainer to ensure single-cell suspensions, and processed immediately for library preparation. For the EED226 experiments, 4-week-old *Isl1-nLacZ* male and female mice were used (n = 4), and each sample was cultured separately (in triplicate) for 5 days, in the presence or absence of 10 μM EED226.

scRNAseq analysis

scRNAseq was performed as described before (*39*). Briefly, the dorsal and ventral scRNAseq libraries were prepared with the 10x Chromium

system, using the Chromium Single Cell 3′ (v3 chemistry) kit, according to the manufacturers' instructions, and sequenced in an Illumina NovaSeq 6000 at the University of Miami, Sylvester Comprehensive Cancer Center, Oncogenomics Core Facility. Raw base call (BCL) files were analyzed using Cell Ranger. The "mkfastq" command was used to generate FASTQ files, and the "count" command was used to generate raw gene-barcode matrices aligned to the Mm10 Ensembl build 93 genome. The data from both samples were combined in R using the Seurat package, and an aggregate Seurat object was generated (*40*). To ensure that our analysis was on high-quality cells, filtering was conducted by retaining cells that had unique molecular identifiers greater than 400, expressed 100 to 8000 genes. This resulted in 9893 cells for dorsal and 11,418 cells for ventral. Data from each sample were analyzed using the SCTransform Integration Workflow (https://satijalab.org/seurat/v3.0/integration.html). Data from each sample were normalized using the SCTransform() function, and integration features were identified using SelectIntegrationFeatures() with "nfeatures" and "fvf.nfeatures" set to 5000. To identify integration anchor genes among the two samples, the PrepSCTIntegration() and FindIntegrationAnchors() functions were used with 5000 genes. Using Seurat's IntegrateData(), the samples were combined into one object. To reduce dimensionality of this dataset, principal components analysis (PCA) was used, and the first 10 principal components were further summarized using UMAP dimensional reduction. The DimPlot() function was used to generate the UMAP plots displayed. Clustering was conducted using the FindNeighbors() and FindClusters() functions using the original Louvain algorithm, 10 PCA components, and a resolution parameter set to 0.5. The resulting 15 Louvain clusters were visualized in a two-dimensional UMAP representation and were annotated to known biological cell types using canonical marker genes, as well as GSEA (Enrichr, https://amp.pharm.mssm.edu/Enrichr/).The DoHeatmap() command was used to generate the heatmap displayed, and the VlnPlot() command was used to generate violin plots of the Louvain clusters.

Single-cell trajectory reconstruction

Single-cell pseudotime trajectories were constructed with Monocle 2 (*26*). For the analysis, we used the normalized expression data from the subset expressing *Isl1* or *Nkx2-5* greater than 0 to infer the relationship between these cell types. Using these criteria, 868 cells entered the Monocle2 analysis. Genes for trajectory inference were selected using the dispersionTable() function to calculate a smooth function describing how variance in each gene's expression across cells varies according to the mean. A total of 5051 genes with a mean expression greater than or equal to 0.1 were used for the analysis. The reduceDimension() function was used with the DDRTree reduction method, and the following parameters were modified: ncenter = 100, max_components = 3, and num_dim = 10. Results were visualized using the plot_cell_trajectory() or plot_complex_cell_trajectory function and annotated with the corresponding cell type. BEAM (branched expression analysis modeling) was used for branched-dependent gene expression analysis (*26*).

Statistical analysis

The scRNAseq data were analyzed in RStudio using the Seurat (*40*) and Monocle (*26*) packages, as described above. For differential expression analysis in Seurat, the default two-sided nonparametric Wilcoxon rank sum test was used. Trajectory-dependent differential expression analysis was conducted with Monocle's BEAM. Functional enrichment analysis of the DEGs was conducted with G: Profiler (https://biit.cs.ut.ee/gprofiler/gost) and GSEA (www.gsea-msigdb.org). All other statistical tests were performed in GraphPad Prism (version 8, La Jolla, CA) using Student's *t* test, Mann-Whitney test, or one-way analysis of variance (ANOVA) followed by Tukey's post hoc tests. All data met the assumptions of the tests (Bartlett's test for normality). A P value of <0.05 was considered statistically significant. All values are reported as means ± SEM.

SUPPLEMENTARY MATERIALS

Supplementary material for this article is available at http://advances.sciencemag.org/cgi/content/full/6/49/eaba9950/DC1

View/request a protocol for this paper from *Bio-protocol*.

REFERENCES AND NOTES

1. O. W. J. Prall, M. K. Menon, M. J. Solloway, Y. Watanabe, S. Zaffran, F. Bajolle, C. Biben, J. J. McBride, B. R. Robertson, H. Chaulet, F. A. Stennard, N. Wise, D. Schaft, O. Wolstein, M. B. Furtado, H. Shiratori, K. R. Chien, H. Hamada, B. L. Black, Y. Saga, E. J. Robertson, M. E. Buckingham, R. P. Harvey, An Nkx2-5/Bmp2/Smad1 negative feedback loop controls heart progenitor specification and proliferation. *Cell* **128**, 947–959 (2007).
2. C.-L. Cai, X. Liang, Y. Shi, P.-H. Chu, S. L. Pfaff, J. Chen, S. Evans, Isl1 identifies a cardiac progenitor population that proliferates prior to differentiation and contributes a majority of cells to the heart. *Dev. Cell* **5**, 877–889 (2003).
3. S. M. Meilhac, M. E. Buckingham, The deployment of cell lineages that form the mammalian heart. *Nat. Rev. Cardiol.* **15**, 705–724 (2018).
4. J. Kang, E. Nathan, S.-M. Xu, E. Tzahor, B. L. Black, Isl1 is a direct transcriptional target of Forkhead transcription factors in second-heart-field-derived mesoderm. *Dev. Biol.* **334**, 513–522 (2009).
5. C. Kappen, J. M. Salbaum, Identification of regulatory elements in the Isl1 gene locus. *Int. J. Dev. Biol.* **53**, 935–946 (2009).
6. S. M. Meilhac, R. G. Kelly, D. Rocancourt, S. Eloy-Trinquet, J.-F. Nicolas, M. E. Buckingham, A retrospective clonal analysis of the myocardium reveals two phases of clonal growth in the developing mouse heart. *Development* **130**, 3877–3889 (2003).
7. R. E. Poelmann, A. C. Gittenberger-de Groot, A subpopulation of apoptosis-prone cardiac neural crest cells targets to the venous pole: Multiple functions in heart development? *Dev. Biol.* **207**, 271–286 (1999).
8. V. Hildreth, S. Webb, L. Bradshaw, N. A. Brown, R. H. Anderson, D. J. Henderson, Cells migrating from the neural crest contribute to the innervation of the venous pole of the heart. *J. Anat.* **212**, 1–11 (2008).
9. T. Nakamura, M. C. Colbert, J. Robbins, Neural crest cells retain multipotential characteristics in the developing valves and label the cardiac conduction system. *Circ. Res.* **98**, 1547–1554 (2006).
10. K. E. Hatzistergos, L. M. Takeuchi, D. Saur, B. Seidler, S. M. Dymecki, J. J. Mai, I. A. White, W. Balkan, R. M. Kanashiro-Takeuchi, A. V. Schally, J. M. Hare, cKit$^+$ cardiac progenitors of neural crest origin. *Proc. Natl. Acad. Sci. U.S.A.* **112**, 13051–13056 (2015).
11. W. Tang, M. L. Martik, Y. Li, M. E. Bronner, Cardiac neural crest contributes to cardiomyocytes in amniotes and heart regeneration in zebrafish. *eLife* **8**, e47929 (2019).
12. S. Abdul-Wajid, B. L. Demarest, H. J. Yost, Loss of embryonic neural crest derived cardiomyocytes causes adult onset hypertrophic cardiomyopathy in zebrafish. *Nat. Commun.* **9**, 4603 (2018).
13. M. Sande-Melon, I. J. Marques, M. Galardi-Castilla, X. Langa, M. Pérez-López, M.-A. Botos, H. Sánchez-Iranzo, G. Guzmán-Martínez, D. M. Ferreira Francisco, D. Pavlinic, V. Benes, R. Bruggmann, N. Mercader, Adult sox10$^+$ cardiomyocytes contribute to myocardial regeneration in the zebrafish. *Cell Rep.* **29**, 1041–1054.e5 (2019).
14. Y. Sun, X. Liang, N. Najafi, M. Cass, L. Lin, C.-L. Cai, J. Chen, S. M. Evans, Islet 1 is expressed in distinct cardiovascular lineages, including pacemaker and coronary vascular cells. *Dev. Biol.* **304**, 286–296 (2007).
15. Y. Li, Z. Lv, L. He, X. Huang, S. Zhang, H. Zhao, W. Pu, Y. Li, W. Yu, L. Zhang, X. Liu, K. Liu, J. Tang, X. Tian, Q.-D. Wang, K. O. Lui, B. Zhou, Genetic tracing identifies early segregation of the cardiomyocyte and nonmyocyte lineages. *Circ. Res.* **125**, 343–355 (2019).
16. K.-L. Laugwitz, A. Moretti, J. Lam, P. Gruber, Y. Chen, S. Woodard, L.-Z. Lin, C.-L. Cai, M. M. Lu, M. Reth, O. Platoshyn, J. X.-J. Yuan, S. Evans, K. R. Chien, Postnatal isl1$^+$ cardioblasts enter fully differentiated cardiomyocyte lineages. *Nature* **433**, 647–653 (2005).
17. H. Honkoop, D. E. M. de Bakker, A. Aharonov, F. Kruse, A. Shakked, P. D. Nguyen, C. de Heus, L. Garric, M. J. Muraro, A. Shoffner, F. Tessadori, J. C. Peterson, W. Noort,

A. Bertozzi, G. Weidinger, G. Posthuma, D. Grun, W. J. van der Laarse, J. Klumperman, R. T. Jaspers, K. D. Poss, A. van Oudenaarden, E. Tzahor, J. Bakkers, Single-cell analysis uncovers that metabolic reprogramming by ErbB2 signaling is essential for cardiomyocyte proliferation in the regenerating heart. *eLife* **8**, e50163 (2019).
18. K. A. Engleka, L. J. Manderfield, R. D. Brust, L. Li, A. Cohen, S. M. Dymecki, J. A. Epstein, Islet1 derivatives in the heart are of both neural crest and second heart field origin. *Circ. Res.* **110**, 922–926 (2012).
19. J. N. Domínguez, S. M. Meilhac, Y. S. Bland, M. E. Buckingham, N. A. Brown, Asymmetric fate of the posterior part of the second heart field results in unexpected left/right contributions to both poles of the heart. *Circ. Res.* **111**, 1323–1335 (2012).
20. A. He, Q. Ma, J. Cao, A. von Gise, P. Zhou, H. Xie, B. Zhang, M. Hsing, D. C. Christodoulou, P. Cahan, G. Q. Daley, S. W. Kong, S. H. Orkin, C. E. Seidman, J. G. Seidman, W. T. Pu, Polycomb repressive complex 2 regulates normal development of the mouse heart. *Circ. Res.* **110**, 406–415 (2012).
21. W. Qi, K. Zhao, J. Gu, Y. Huang, Y. Wang, H. Zhang, M. Zhang, J. Zhang, Z. Yu, L. Li, L. Teng, S. Chuai, C. Zhang, M. Zhao, H. Chan, Z. Chen, D. Fang, Q. Fei, L. Feng, L. Feng, Y. Gao, H. Ge, X. Ge, G. Li, A. Lingel, Y. Lin, Y. Liu, F. Luo, M. Shi, L. Wang, Z. Wang, Y. Yu, J. Zeng, C. Zeng, L. Zhang, Q. Zhang, S. Zhou, C. Oyang, P. Atadja, E. Li, An allosteric PRC2 inhibitor targeting the H3K27me3 binding pocket of EED. *Nat. Chem. Biol.* **13**, 381–388 (2017).
22. P. Khattar, F. W. Friedrich, G. Bonne, L. Carrier, T. Eschenhagen, S. M. Evans, K. Schwartz, M. Y. Fiszman, J.-T. Vilquin, Distinction between two populations of islet-1-positive cells in hearts of different murine strains. *Stem Cells Dev.* **20**, 1043–1052 (2011).
23. J. Wang, S. B. Greene, M. Bonilla-Claudio, Y. Tao, J. Zhang, Y. Bai, Z. Huang, B. L. Black, F. Wang, J. F. Martin, Bmp signaling regulates myocardial differentiation from cardiac progenitors through a MicroRNA-mediated mechanism. *Dev. Cell* **19**, 903–912 (2010).
24. L. Caputo, H. R. Witzel, P. Kolovos, S. Cheedipudi, M. Looso, A. Mylona, W. F. J. van IJcken, K.-L. Laugwitz, S. M. Evans, T. Braun, E. Soler, F. Grosveld, G. Dobreva, The Isl1/Ldb1 complex orchestrates genome-wide chromatin organization to instruct differentiation of multipotent cardiac progenitors. *Cell Stem Cell* **17**, 287–299 (2015).
25. H. J. Snippert, L. G. van der Flier, T. Sato, J. H. van Es, M. van den Born, C. Kroon-Veenboer, N. Barker, A. M. Klein, J. van Rheenen, B. D. Simons, H. Clevers, Intestinal crypt homeostasis results from neutral competition between symmetrically dividing Lgr5 stem cells. *Cell* **143**, 134–144 (2010).
26. X. Qiu, A. Hill, J. Packer, D. Lin, Y.-A. Ma, C. Trapnell, Single-cell mRNA quantification and differential analysis with Census. *Nat. Methods* **14**, 309–315 (2017).
27. A. E. Lewis, H. N. Vasudevan, A. K. O'Neill, P. Soriano, J. O. Bush, The widely used Wnt1-Cre transgene causes developmental phenotypes by ectopic activation of Wnt signaling. *Dev. Biol.* **379**, 229–234 (2013).
28. K. E. Hatzistergos, Z. Jiang, K. Valasaki, L. M. Takeuchi, W. Balkan, P. Atluri, D. Saur, B. Seidler, N. Tsinoremas, D. L. DiFede, J. M. Hare, Simulated microgravity impairs cardiac autonomic neurogenesis from neural crest cells. *Stem Cells Dev.* **27**, 819–830 (2018).
29. Y. Sun, I. M. Dykes, X. Liang, S. R. Eng, S. M. Evans, E. E. Turner, A central role for Islet1 in sensory neuron development linking sensory and spinal gene regulatory programs. *Nat. Neurosci.* **11**, 1283–1293 (2008).
30. M.-R. Song, Y. Sun, A. Bryson, G. N. Gill, S. M. Evans, S. L. Pfaff, Islet-to-LMO stoichiometries control the function of transcription complexes that specify motor neuron and V2a interneuron identity. *Development* **136**, 2923–2932 (2009).
31. S. Zhuang, Q. Zhang, T. Zhuang, S. M. Evans, X. Liang, Y. Sun, Expression of Isl1 during mouse development. *Gene Expr. Patterns* **13**, 407–412 (2013).
32. N. Guimarães-Camboa, J. Stowe, I. Aneas, N. Sakabe, P. Cattaneo, L. Henderson, M. S. Kilberg, R. S. Johnson, J. Chen, A. D. McCulloch, M. A. Nobrega, S. M. Evans, A. C. Zambon, HIF1α represses cell stress pathways to allow proliferation of hypoxic fetal cardiomyocytes. *Dev. Cell* **33**, 507–521 (2015).
33. R. Fukuda, A. Aharonov, Y. T. Ong, O. A. Stone, M. El-Brolosy, H.-M. Maischein, M. Potente, E. Tzahor, D. Y. R. Stainier, Metabolic modulation regulates cardiac wall morphogenesis in zebrafish. *eLife* **8**, e50161 (2019).
34. F. Weinberger, D. Mehrkens, F. W. Friedrich, M. Stubbendorff, X. Hua, J. C. Muller, S. Schrepfer, S. M. Evans, L. Carrier, T. Eschenhagen, Localization of Islet-1–positive cells in the healthy and infarcted adult murine heart. *Circ. Res.* **110**, 1303–1310 (2012).
35. S. C. van den Brink, F. Sage, A. Vértesy, B. Spanjaard, J. Peterson-Maduro, C. S. Baron, C. Robin, A. van Oudenaarden, Single-cell sequencing reveals dissociation-induced gene expression in tissue subpopulations. *Nat. Methods* **14**, 935–936 (2017).
36. A.-C. Villani, R. Satija, G. Reynolds, S. Sarkizova, K. Shekhar, J. Fletcher, M. Griesbeck, A. Butler, S. Zheng, S. Lazo, L. Jardine, D. Dixon, E. Stephenson, E. Nilsson, I. Grundberg, D. McDonald, A. Filby, W. Li, P. L. De Jager, O. Rozenblatt-Rosen, A. A. Lane, M. Haniffa, A. Regev, N. Hacohen, Single-cell RNA-seq reveals new types of human blood dendritic cells, monocytes, and progenitors. *Science* **356**, eaah4573 (2017).
37. X. Liu, W. Chen, W. Li, Y. Li, J. R. Priest, B. Zhou, J. Wang, Z. Zhou, Single-cell RNA-seq of the developing cardiac outflow tract reveals convergent development of the vascular smooth muscle cells. *Cell Rep.* **28**, 1346–1361.e4 (2019).
38. M. Asp, S. Giacomello, L. Larsson, C. Wu, D. Fürth, X. Qian, E. Wärdell, J. Custodio, J. Reimegård, F. Salmén, C. Österholm, P. L. Ståhl, E. Sundström, E. Åkesson, O. Bergmann, M. Bienko, A. Månsson-Broberg, M. Nilsson, C. Sylvén, J. Lundeberg, A spatiotemporal organ-wide gene expression and cell atlas of the developing human heart. *Cell* **179**, 1647–1660.e19 (2019).
39. M. A. Durante, S. Kurtenbach, Z. B. Sargi, J. W. Harbour, R. Choi, S. Kurtenbach, G. M. Goss, H. Matsunami, B. J. Goldstein, Single-cell analysis of olfactory neurogenesis and differentiation in adult humans. *Nat. Neurosci.* **23**, 323–326 (2020).
40. T. Stuart, A. Butler, P. Hoffman, C. Hafemeister, E. Papalexi, W. M. Mauck III, Y. Hao, M. Stoeckius, P. Smibert, R. Satija, Comprehensive integration of single-cell data. *Cell* **177**, 1888–1902.e21 (2019).

Acknowledgments: We thank S. M. Evans from the Skaggs School of Pharmacy and Pharmaceutical Sciences, UCSD, La Jolla, CA, USA and C. Cai from the Icahn School of Medicine at Mount Sinai, NY, USA for providing the *Isl1-nLacZ* mice. We thank S. Wu from Stanford University School of Medicine for critically reviewing our manuscript. We thank the MMRRC for the cryopreserved *Mef2c-AHF-Cre* material. We also thank the ENCODE Consortium and the ENCODE production laboratory of B. Ren at UCSD for generating the ChIP-seq datasets. We acknowledge the support of the Biostatistics and Bioinformatics and Oncogenomics Shared Resources at the Sylvester Comprehensive Cancer Center and the Center for Computational Science High Performance Computing Group at the University of Miami. **Funding:** This work was supported by the NIH grants R01 HL107110, R01 HL094849, R01 HL110737, R01 HL084275, and 5UM HL113460; grants from the Starr Foundation; and the Soffer Family Foundation (all awarded to J.M.H.). This work was further supported by R01 CA125970 (to J.W.H.), a University of Miami Medical Scientist Training Program (to M.A.D.), the Sheila and David Fuente Graduate Program in Cancer Biology (to M.A.D.), a Center for Computational Science Fellowship (to M.A.D.), and a gift from M. J. Daily (to J.W.H.). The Sylvester Comprehensive Cancer Center also received funding from the National Cancer Institute Core Support grant P30 CA240139. The Bascom Palmer Eye Institute also received funding from NIH Core Grant P30EY014801 and a Research to Prevent Blindness Unrestricted Grant. The content is solely the responsibility of the authors and does not necessarily represent the official views of the NIH. **Author contributions:** K.E.H. conceived the project, performed experiments, analyzed and interpreted the data, and wrote the manuscript. M.A.D. analyzed and interpreted the data and edited the manuscript. K.V. performed experiments, analyzed the data, and edited the manuscript. J.W.H. and J.M.H. provided resources, interpreted the data, and wrote the manuscript. A.C.B.A.W. performed experiments and analyzed data. **Competing interests:** J.M.H. is the chief scientific officer, a compensated consultant, and advisory board member for Longeveron and holds equity in Longeveron. J.M.H. is also the co-inventor of intellectual property licensed to Longeveron. J.M.H. also discloses a relationship with Vestion Inc. that includes equity, board membership, and consulting. K.E.H. discloses a relationship with Vestion Inc. that includes equity. K.E.H. and J.M.H. are also the co-inventors of intellectual property licensed to Vestion. J.W.H. is the inventor of intellectual property not discussed in this study. J.W.H. is a paid consultant for Castle Biosciences, is a licensee of this intellectual property, and receives royalties from its commercialization. No other authors declare a potential competing interest. Vestion Inc., Longeveron, and Castle Biosciences did not participate in funding this work. **Data and materials availability:** Next-generation sequencing data are available through the Gene Expression Omnibus (GEO; accession number GSE139168). All custom code is available from the authors upon request. The *Isl1-nLacZ* mice can be provided by J.M.H. pending written permission by the University of California San Diego, scientific review, and a completed material transfer agreement. Requests for the *Isl1-nLacZ* mice should be submitted to J.M.H. at jhare@miami.edu.

Submitted 27 January 2020
Accepted 20 October 2020
Published 2 December 2020
10.1126/sciadv.aba9950

Citation: K. E. Hatzistergos, M. A. Durante, K. Valasaki, A. C. B. A. Wanschel, J. W. Harbour, J. M. Hare, A novel cardiomyogenic role for Isl1^{+} neural crest cells in the inflow tract. *Sci. Adv.* **6**, eaba9950 (2020).